

## Experimental Investigation on Heat Spreader Integrated Microchannel Using Graphene Oxide Nanofluid

Ganesan Narendran, Nagarajan Gnanasekaran & Dharmaraj Arumuga Perumal

To cite this article: Ganesan Narendran, Nagarajan Gnanasekaran & Dharmaraj Arumuga Perumal (2019): Experimental Investigation on Heat Spreader Integrated Microchannel Using Graphene Oxide Nanofluid, Heat Transfer Engineering, DOI: [10.1080/01457632.2019.1637136](https://doi.org/10.1080/01457632.2019.1637136)

To link to this article: <https://doi.org/10.1080/01457632.2019.1637136>



Published online: 12 Aug 2019.



Submit your article to this journal [↗](#)



Article views: 40



View related articles [↗](#)



View Crossmark data [↗](#)

# Experimental Investigation on Heat Spreader Integrated Microchannel Using Graphene Oxide Nanofluid

Ganesan Narendran, Nagarajan Gnanasekaran, and Dharmaraj Arumuga Perumal

Department of Mechanical Engineering, National Institute of Technology Karnataka, Surathkal, India

## ABSTRACT

Thermal design consideration is highly essential for efficient heat dissipation in advanced microprocessors which are subjected to conjugate heat transfer under high heat flux with a minimal area for cooling. Generally, these multicore processors develop a localized high density heat flux referred to as hotspot. The effective use of microchannel in order to mitigate the hotspot is found in literature; however, the flow induced hotspot still exist due to maldistribution of flow inside the microchannel. Henceforth, the present study provides an experimental insight on laminar forced convection in a parallel microchannel heat sink accompanied with 1.2 mm thin copper heat spreader with a surface area of 30 mm<sup>2</sup> to effectively migrate the maldistribution flow induced hot spot. The present experimental study provides a profound insight about the hotspot and migration of hotspot to safe zones; as a result, not only the performance of the multi core microprocessor is highly improved but also the reliability of neighboring components is well secured.

## Introduction

The rapid advancement in the field of consumer electronics has paved the way for reduction in size of the transistors with increased switching frequency and efficiency for better packaging and performance. But the level of downsizing has developed bottleneck to the functionality of the transistor and caused limitations to Moore's law [1]. However, introduction of three dimensional multiple gate transistors enabled further miniaturization to develop transistors with reduced leakage current and power consumption. But still, the electronic chips generate heat flux greater than 80 W/cm<sup>2</sup> which makes the system thermally unstable [2]. To avoid this situation, an optimal thermal dissipation design of cooling systems with efficient packaging must be conceived. The most effective thermal management is delivered by microchannel heat sink which was first introduced by Tuckerman and Pease [3]. This initiated several researchers to perform investigations on different types of the channel cross sections with various working fluids [4–8]. McHale and Garimella [9] presented numerical analysis in trapezoidal microchannel with various aspect ratios. They varied the aspect ratio and side wall angle

of the trapezoidal channel and found improvement in heat transfer characteristics. Wu and Cheng [10] performed experimental and numerical studies in smooth trapezoidal silicon microchannel with different aspect ratios. Glazar *et al.* [11] studied compact heat exchangers with different shapes of microchannel. They concluded that the shape of microchannel influences the effectiveness of heat transfer and pressure drop. Additionally, they reported that excellent results were accomplished when the shapes of the microchannel were diamond and hexagon.

Subsequently, further improvement in microchannel heat sink was found with high thermal conductive fluids that show better stability and significant enhancement in heat transfer for a small dispersion of nano size metallic or oxide particle in the base fluid [12]. Koo and Kleinstreuer [13] performed conjugate heat transfer analysis in a rectangular microchannel heat sink with high thermal conductivity of CuO/Water and CuO/Ethylene Glycol nanofluid. Numerical study on conjugate heat transfer in a rectangular microchannel heat sink with Al<sub>2</sub>O<sub>3</sub>/water nanofluid was performed by Bhattacharya *et al.* [14]. They reported the effects of nanoparticle concentration on Reynolds number and the performance of



**Table 1.** Summary of heat spreader investigations integrated with microchannel heat sink.

	Authors	Study type	Performed investigation	Outcomes
1	Soliman and Hassan [31]	Numerical	Use of microchannel with heat spreader to enhance the solar cell performance. The presented approach uses microchannel below the heat spreader.	Adding, heat spreader to the microchannel developed lowest temperature to the solar cell and improved solar cell efficiency and electrical output than the system only with microchannel.
2	Soliman <i>et al.</i> [32]	Analytical and Numerical	Mathematical approach dedicated to analyze the constructive effects of heat spreader. The presented approach uses microchannel at the bottom of the heat spreader.	The presented model showed 15 °C lower temperature in photovoltaic solar cell module. Result showed 9% increase in photovoltaic output efficiency by using heat spreader.
3	Lee <i>et al.</i> [33]	Experimental	It uses three-dimensional printed heat spreader for liquid cooling of laser driven head lamp. Analysis incorporated the flow pass through the heat spreader.	With the use of heat spreader higher performance was developed comparatively better than thermoelectric cooling.
4	Kelly <i>et al.</i> [34]	Experimental	Use of fractal pulsating heat pipe in heat spreader to perform thermal management for hotspots in electronic components. In this case the radial pulsating pipe is present in the heat spreader itself.	Result showed effective thermal spreading of hotspot. The study presented results in decrease in temperature by 23 °C for the case of 30W heater power.
5	Han <i>et al.</i> [35]	Experimental and Numerical	Investigated hotspot cooling using diamond heat spreader accompanied with Gallium nitride (GaN) heat sink.	Adding diamond heat spreader the maximum heater temperature reduces up to 22.9%.

glycol base fluid using two-step process and observed improvement in thermal conductivity of the nanofluid by 61% with enhanced stability. Zubir *et al.* [17] established a 25% enhancement in thermal conductivity using reduced GO nanofluid with an increase in viscosity by 4% with water as base fluid.

Siva *et al.* [18] conducted experimental and numerical studies on flow configurations to reduce hotspots in parallel microchannel. They observed that the highly distributed flow develops more pressure drop with decreased average temperature in channels. Kumaraguruparan *et al.* [19] reported flow distribution and fluid recirculation on *U*-type flow configuration and they insist that the fluid maldistribution increases at larger mass flow rate for higher heat flux condition. Investigations on the shapes of the flow header for different flow configuration were performed by Kumaran *et al.* [20]. They observed better flow distribution using triangular header for inlet and trapezoidal header for outlet. Solovitz [21] reported analytical studies on flow distribution in parallel microchannel with stepped inlet/outlet manifolds and showed that hotspots can be controlled by using stepped manifolds with low Reynolds number.

Maganti *et al.* [22] performed experimental studies on parallel microchannel accompanied with heat spreader for cooling of micro-electro-mechanical-devices. Their study investigated the flow maldistribution for different flow configurations with the use of high

thermal conductive nanofluid. Maganti *et al.* [23] used graphene nanofluid to mitigate the hotspots in parallel microchannel. They observed more uniform cooling with nanofluid than pure fluids. Anbumeenachi and Thanasekar [24] examined the influence of header shape on flow maldistribution in microchannels. They observed that, the rectangular header design generates lesser flow maldistribution at increased flow rates. Numerical investigation on electronic components with micropin fins subjected to hotspot was reported by Reddy and Dulikravich [25]. They performed multi-objective optimization to determine the optimal working condition by minimizing hotspot temperature and pumping power. Further, they reported the structural stress experienced by the micropin fin arrays due to hotspots. Sharma *et al.* [26] conducted experimental study with novel slot nozzles to reduce hotspots for embedded electronic systems. They were able to bring down the sink temperature to 4 °C and hot spot temperature to 15 °C using the slot nozzle design. Alfieri *et al.* [27] performed numerical investigations on hotspots in three-dimensional stacked chips using integrated cooling. It has been found that the hotspots identified near the inlet region of the channel develop better uniform sink temperature with reduced average Nusselt number.

Zhang *et al.* [28] investigated transient cooling in electronic chip with different types of microchannel heat sinks by both experimentally and numerically.

According to them, the straight channels have comparatively higher response timing than *U*-shaped and serpentine type channels. Additionally, they reported that reduction in response timing was observed for increased flow rate. Kinkelin *et al.* [29] performed experimental and numerical studies on peak temperature loading under transient chip cooling application by using hybrid heat spreader with combined carbon nanotubes and phase change materials.

From the available literature, it is understood that the hotspots are predominately developed in multicore processors which are potentially capable of developing thermal imbalance which in turn reduces the reliability of miniaturized electronic components. Moreover, ineffective cooling systems can further intensify the effects of hotspot. In many cases, the hotspot problems were approached by methods like implementing embedded cooling, involving liquid cooling with high thermal conductive fluids containing metallic nanoparticle, minimizing the hotspot by well optimized manifold design and use of heat spreaders with direct contact on high heat flux generating systems. In practice, it has been observed that the high heat flux density, which is responsible for hotspot, is spontaneous and instantaneously varies with time and space. It is pertinent to mention that to the best of the authors' knowledge experimental investigations on compact fluid handling unit accompanied with very large surface heat spreader for the solution of effective cooling was not examined adequately in the literature. Therefore, a holistic approach has been presented in this work in order to mitigate the hotspot to a maximum level using a compact fluid handling unit dedicated to microchannel with a thin heat spreader involving 0.02–0.12 vf % of GO based working fluid.

## Approach

### Background of the study

With the introduction of ultra large scale integration technology, millions of electronic components can be integrated within small area to develop high performance devices [30]. Under these high end packaging circumstances, it is highly incompatible to accommodate conventional single phase cooling technologies. Additionally, latest processors have multiple cores which operate according to the computational loads. It is quite difficult and challenging to design a microchannel heat sink to match varying thermal loads of the processor. One way of solving this situation is by using different flow patterns in a single microchannel

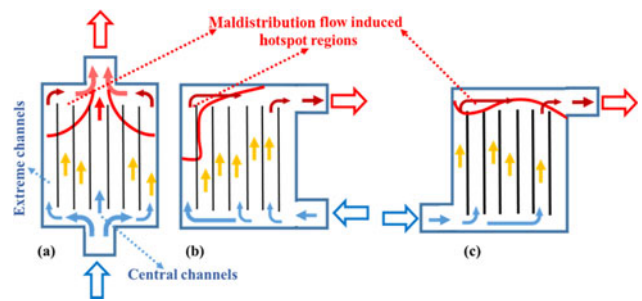


**Figure 1.** Standard flow configuration. (a) I-type, (b) C-type and (c) Z-type.

heat sink for different processor load pattern, but this will lead to complex construction of microchannel. An effective way to solve the problem is by adding a heat spreader that acts as a high conductive buffer plate to reduce the peak thermal loads from processor to microchannel. Some of the recent investigations involving heat spreader for thermal management for various applications are listed in Table 1 [31–35]. Primarily flow induced hotspot occurs due to flow maldistribution among the microchannels. More appropriately, the location of flow maldistribution is defined in accordance with the sink design and flow configuration. The most standard flow configuration types are I-type, C-type, and Z-type, refer to Figure 1.

Maldistribution happens due to the non-uniform fluid flow in the microchannels. In the case of I-type parallel microchannels shown in Figure 1(a) the flow rate in the central channels is comparatively higher than the extreme channels. Due to this, the outlet temperature of the extreme channels is higher and there is minimal heat transfer near the outlet region of the microchannels. This gives rise to two symmetric flow maldistribution induced hotspot region near the outlet which is unavoidable in the case of I-type flow. These effects were observed on several other varied configurations of I-type such as rectangular double layer and I-type with pin fins. Similar, results were observed for C and Z-type, shown in Figures 1(b) and (c), at different locations of the heat sinks.

Additionally, the latest liquid cooling modules were directly mounted over the processors and its maximum priority was to maintain a uniform temperature throughout the heat sink. Maganti *et al.* [36] investigated parallel microchannels to mitigate hotspot using different nanofluid. They noticed that the heat sink undergoes two different hotspot types one which developed due to flow maldistribution and other formed by the localized heat flux developed by the device. Investigations on hotspot cooling using different microchannel configurations are summarized in

**Table 2.** Summary of investigations on hotspot management with different techniques.

	Authors	Type of study	Performed investigations	Outcomes
1	Wang <i>et al.</i> [37]	Experimental and Numerical	Investigation of hotspots in densely packed components, as well as decreasing the thermal contact resistance using thermoelectric cooling.	Adding thermoelectric coolers developed significant improvement in cooling hotspots in silicon chips. The results showed that hotspot of 1,250 W/cm <sup>2</sup> heat flux can be reduced to 17°C with 20µm thermoelectric mini contacts.
2	Bar-Cohen and Wang [38]	Experimental and Numerical	On chip thermal management of hotspot using thermoelectric micro coolers and two- phase micro gap coolers.	Their results show that effect of heat spreader is dominant in reducing the hotspot in the absence of thermoelectric cooler. On the operation of thermoelectric generator the hotspot is effectively cooled by the micro cooler. They concluded that to develop a better cooling effect micro cooler must be larger than the hotspot.
3	Ansari and Kim [39]	Numerical	Performed a conjugate heat transfer analysis using hybrid microchannels. Constitutes a combined rectangular microchannel and cylindrical micro fins depending on the thermal loadings.	They presented hybrid heat sink with improved heat transfer performance than normal microchannel subjected to hotspots. The hybrid sink maintains 30.6% lower hotspot temperatures with 11.7% higher pumping power than conventional microchannels.
4	Pi <i>et al.</i> [40]	Experimental	Presented an effective method to estimate the hotspot temperature on multiple hotspot conditions. Simplified model was presented by using superposition method to reduce the computational time by 15%.	Results showed that cooling performance of the device decreased with decrease in hotspot size.
5	Drummond <i>et al.</i> [41]	Experimental	Use of hierarchical manifold based microchannel to dissipate intra chip hotspots. Analysis includes hotspot flux ranging more than 2,500W/cm <sup>2</sup> .	The proposed design developed more uniformity in the chip temperature and maintained an average temperature of 30 °C more than inlet temperature, at a pressure drop of 75 kPa.
6	Abdoli <i>et al.</i> [42]	Numerical	Investigated double layer microchannel for cooling hotspots in electronic components.	Results showed double microchannel configuration effectively dissipated higher hotspot heat flux range of 2,000 W/cm <sup>2</sup> . Recommended heat spreader for higher thermal loads.
7	Lorenzini <i>et al.</i> [43]	Numerical	Investigated embedded microfluidic cooling by implementing micro gaps between pin fin structures for mitigating hotspot.	Results showed that the embedded cooling design effectively maintains the temperature of device below 65 °C with a marginal increase in pressure drop.
8	Lee <i>et al.</i> [44]	Experimental and Numerical	Implemented oblique finned microchannel heat sink to cool the hotspot regions.	Oblique microchannel developed more uniform sink temperature under multiple hotspot conditions.
9	Green <i>et al.</i> [45]	Analytical and Experimental	Presented a chip level thermal management by a compact fluid -to -fluid spot-to -spreader hybrid heat sink.	Results showed effective cooling of hotspot heat flux near 1,000 W/cm <sup>2</sup> .

Table 2 [37–45]. Most importantly from all the three flow configuration cases, maldistribution flow induced hotspots are formed at the outlet region of the heat sink irrespective to the sink design and working fluid. In order to overcome the issue, a high thermal

conductivity plate is attached beneath the microchannel shown in conceptual diagram of Figure 2. Figure 2(a) shows the heat spreader integrated microchannel heat sink. The fluid flow is normal to the microchannel through fluid handling unit (FHU) and exits the

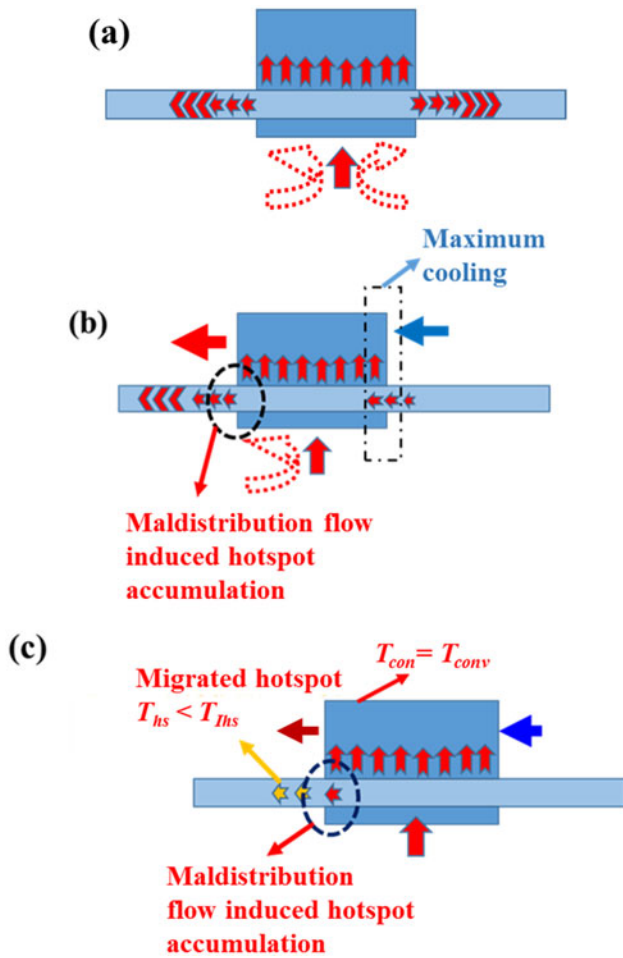


**Figure 2.** Conceptual diagram of microchannel integrated heat spreader approach.

channel. The heat flux from electronic processor is directly applied to the heat sink base, the thermal energy splits evenly on both directions of the heat spreader and majority of the energy is conducted towards the microchannel. Figure 2(b) shows the initiation of the flow, where maximum cooling is observed at the entrance region of the microchannel. Due to this very less conduction happens in the spreader plate near the entrance region. On the other hand, same amount of flux is conducted and get distributed to microchannel and spreader near the exit of the channel. The continuous flow in the microchannel generates an accumulation of flow maldistribution induced hotspot highlighted near the channel exit. The heat capacity of working fluid transports majority of the heat flux conducted from microchannel denoted as  $T_{con} = T_{conv}$  as shown in Figure 2(c). The temperature of the heat spreader is reduced and the peak temperature is at the maldistribution accumulated microchannel exit region. This temperature difference from microchannel to heat spreader allows the

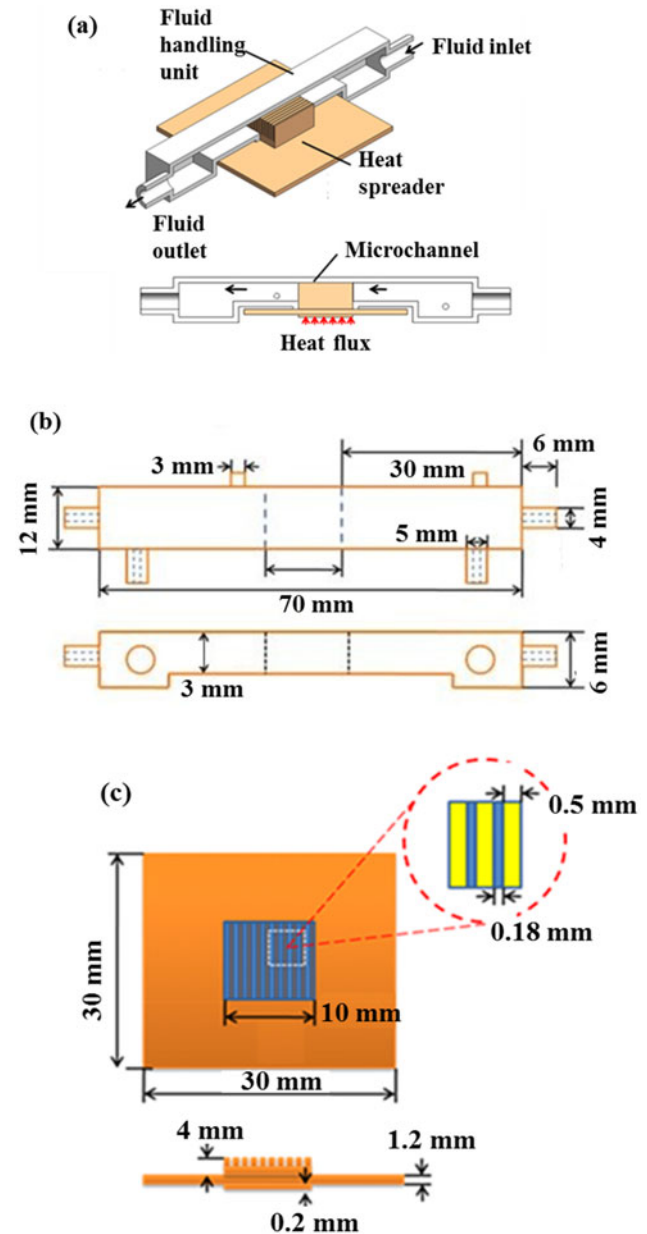


**Figure 3.** Schematic diagram of microchannel integrated heat spreader with dimensions. (a) Section view of the assembly, (b) fluid handling unit and (c) heat spreader dimensions.

thermal energy to migrate in heat spreader which is highlighted as  $T_{hs} < T_{Ihs}$ .

## Experimental setup

### Heat spreader assisted cooling

The major concern of the present heat sink is to mitigate hotspot using heat spreader with the help of compact FHU, so that effective packaging can be implemented. Figure 3 represents the schematic diagram of a microchannel integrated heat spreader.

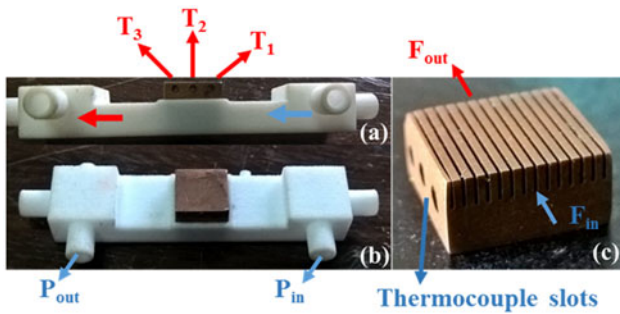


**Figure 4.** Photographs of experimental microchannel module with FHU. (a) microchannel with thermocouple locations, (b) FHU with pressure tapping and (c) microchannel heat sink.

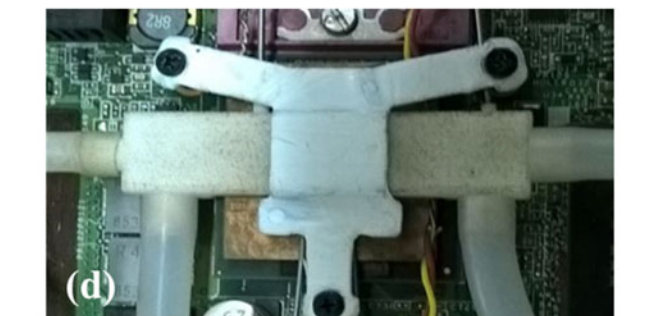
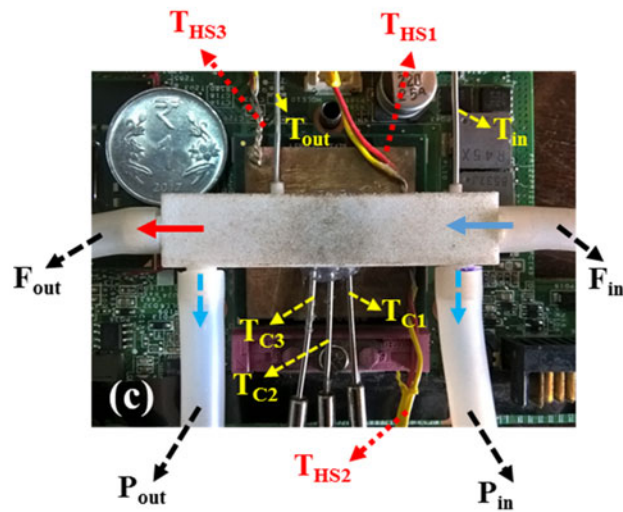
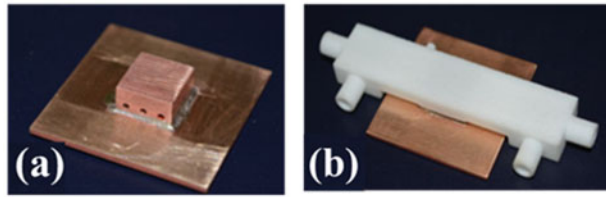


**Figure 5.** Experimental setup of microchannel with heat spreader (a) heat sink (b) heat sink with FHU (c) heat sink with sensors (d) complete module.

**Figure 4** presents the photographs of experimental microchannel module with FHU. Microchannel integrated heat spreader is fabricated as a single piece and

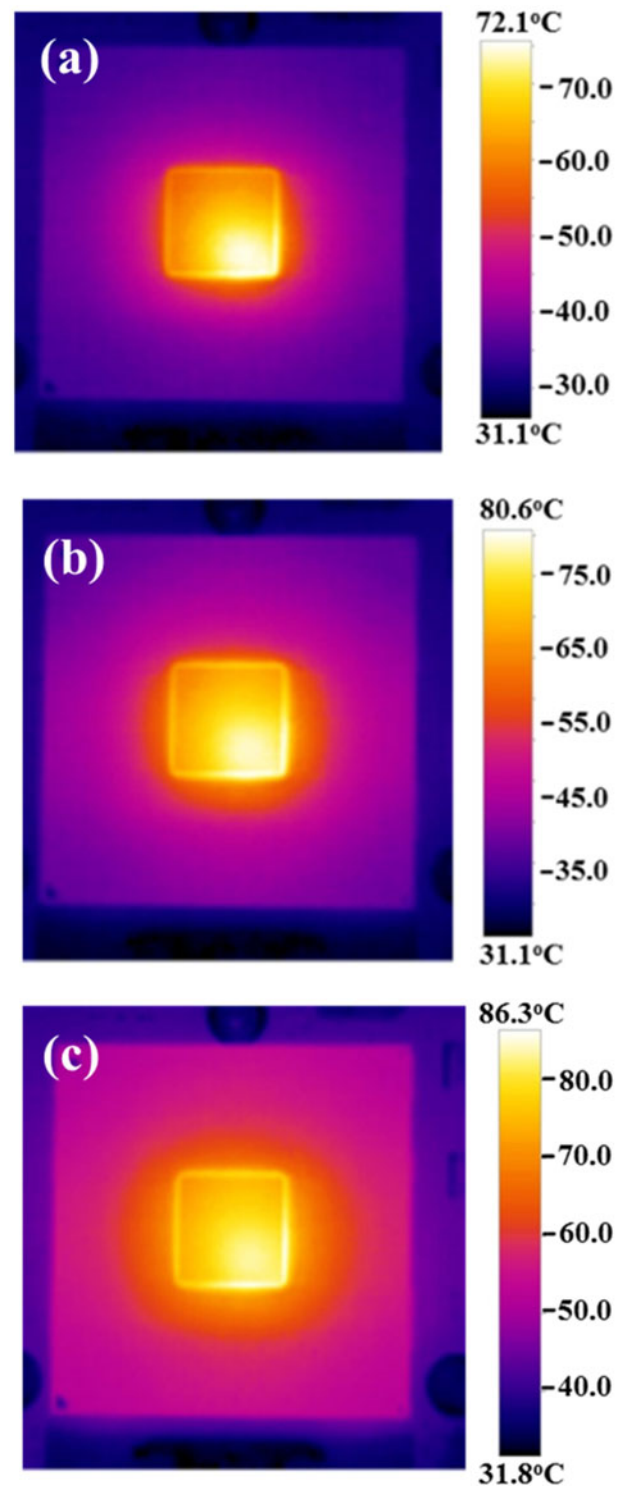


**Figure 6.** Infrared photographs of the processor (a) 8 s, (b) 12 s, and (c) 16 s.

is directly mounted upright to the electronic component. The experimental module of the test setup is shown in **Figure 5**. The FHU is made up of three-dimensional printed high-density acrylonitrile butadiene styrene plastic having fill density of 90% with dedicated orifices for fluid transport and sensing



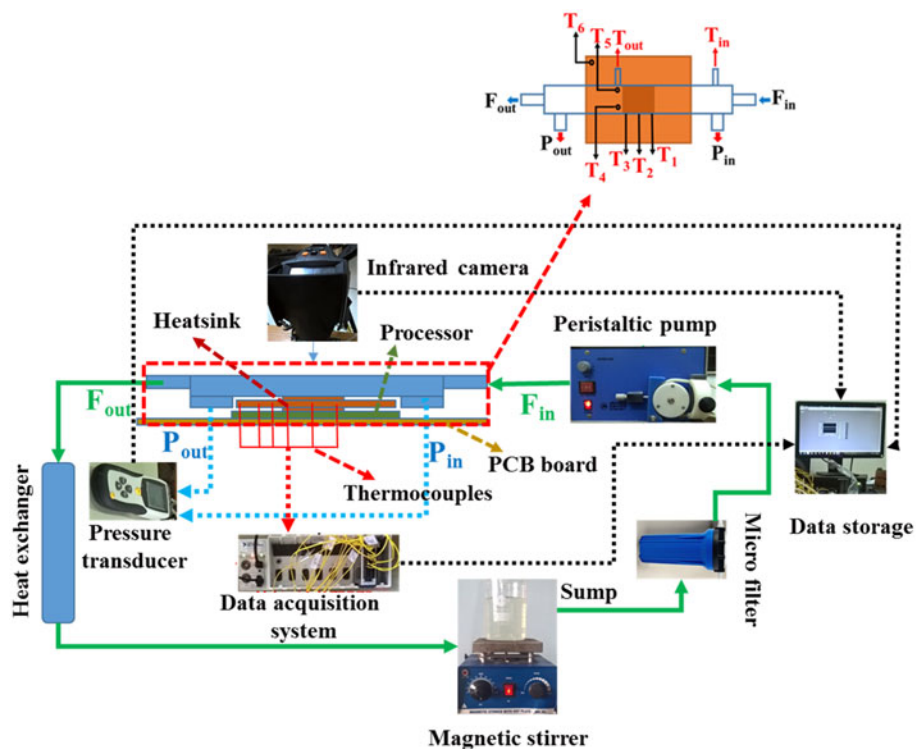


Figure 7. Flow diagram of the experimental setup.

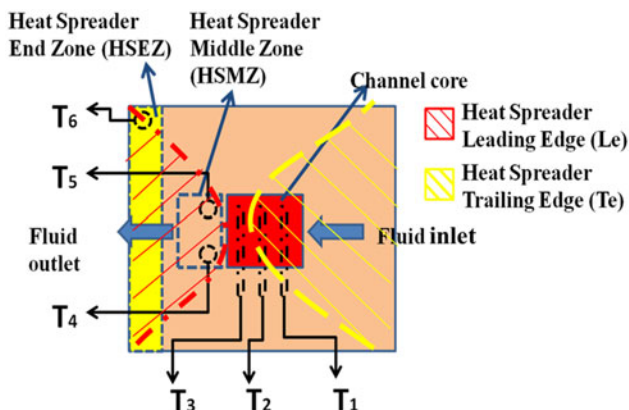


Figure 8. Schematic of thermocouple locations in different temperature zones.

probes. Parallel microchannel with 1 cm length having 14 channels with the height of 2 mm is used to manage the hotspot developed in the processor. The temperature distribution of the dual core processor for progressive timings is shown in Figure 6.

### Description of the experimental facility

The study was carried out on a two core processor (Intel core 2 duo-T7700) with a thermal dissipation power of 35 W. The flow diagram of the experimental test module is shown in Figure 7. The processor and

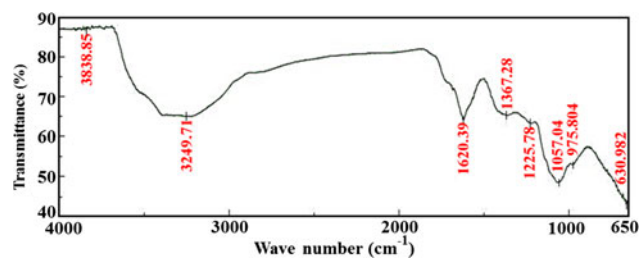
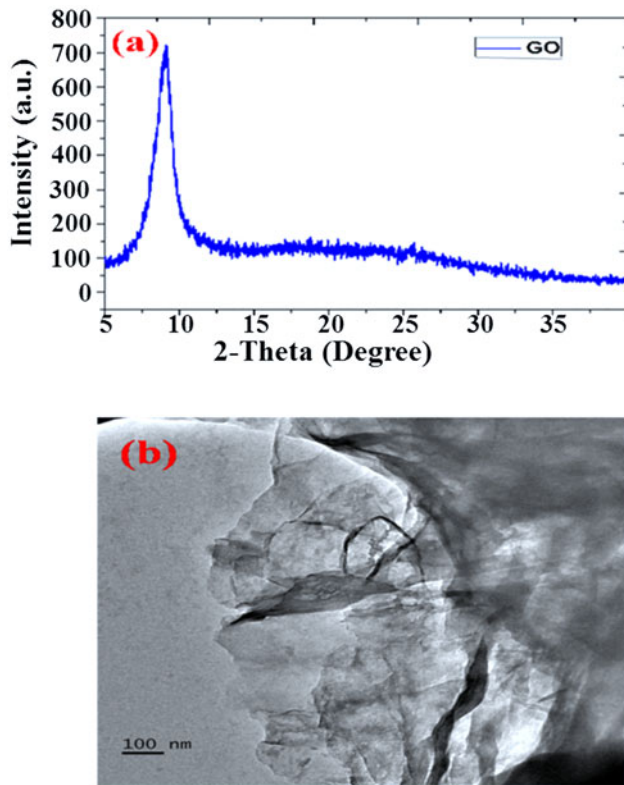


Figure 9. FTIR of GO.

the motherboard are externally controlled and operated at the rated thermal dissipation power. The microchannel set up is integrated with heat spreader and FHU. A peristaltic pump (Murhopye scientific, India) is connected to the FHU to provide a pulsating flow. The outlet is connected to a secondary heat exchanger to reduce the outlet temperature of the working fluid to the room temperature before it is let to the sump which stores the fluid. The fluid is actively stirred in a low RPM for the case of GO nanofluid to stabilize the dispersion of the working fluid. The heat sink is connected with the thermocouples to record the necessary change in temperatures at the inlet and the outlet of the channel. Figure 8 shows the location of thermocouples in different temperature zones of the heat sink. The arrangement is to obtain the temperature distribution of the heat spreader integrated microchannel



**Figure 10.** Characterization images (a) XRD-GO and (b) TEM- GO.

under different mass flow rates and GO volume fraction. The spreader is mainly divided into trailing and leading edges. This corresponds to temperature distribution developed in the spreader plate in accordance to the fluid flow direction. This region is additionally divided into heat spreader end zone (HSEZ) and heat spreader middle zone (HSMZ) to specifically quantify the temperature responses near the outlet of the microchannel ( $T_4$  and  $T_5$ ) and at end of the heat spreader ( $T_6$ ).

## Thermo-physical properties of nanofluids

### Synthesis of graphene oxide and characterization

The procedure for synthesis of GO is followed from Hummers and Offeman's method [46]. On preparation of 1 g of graphite flakes, an equivalent amount of sodium nitrate ( $\text{NaNO}_3$ ) is mixed with 46 mL of  $\text{H}_2\text{SO}_4$  solution. It is kept in the ice bath and stirred until it forms a thick paste. 46 mL of deionized water is added to the paste gradually. Then the step is preceded with 140 mL of deionized water after 30 min and 10 mL of  $\text{H}_2\text{O}_2$  is introduced. This generates a golden yellow precipitate which is then washed with 3% of HCl mixture to remove the impurities. It is

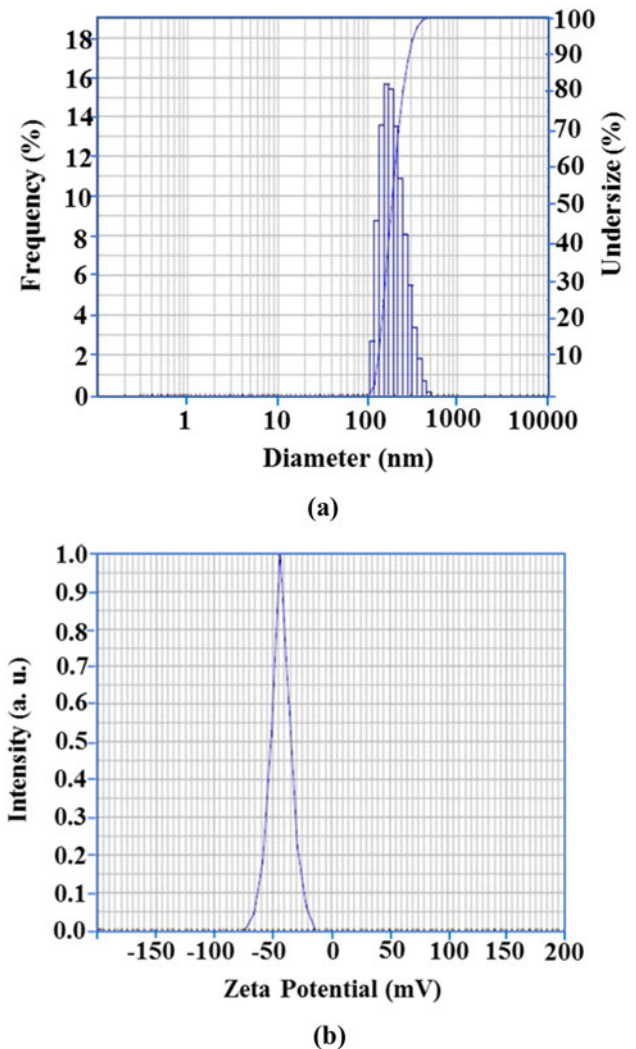


**Figure 11.** Nanofluid stability test (a) Particle size and (b) Zeta potential.

then dried to get GO powder. The GO powder is characterized with tunneling electron microscope (TEM) to observe the morphology of the GO nanoparticles [47]. Fourier transfer infrared spectroscopy (FTIR) is used to characterize the functional group of GO which is shown in Figure 9. The recorded pattern is from 650 to  $4,000\text{ cm}^{-1}$ . The peaks are developed at  $1,057.04\text{ cm}^{-1}$  and  $1,367\text{ cm}^{-1}$  are by formation of  $\text{O}=\text{C}-\text{O}$  and  $\text{C}=\text{O}$  functional groups. The peaks at  $1,620\text{ cm}^{-1}$  corresponds to stretching vibrations of  $\text{C}=\text{O}$  bonds. The peak at  $3,249\text{ cm}^{-1}$  conforms the presence of GO. Figure 10 presents the X-ray diffraction and TEM images of produced GO. Figure 11 shows the average particle size and zeta potential of GO/water nanofluid. Dynamic light scattering technique is used to determine the average particle size which was about 200 nm as shown in Figure 11(a) and zeta potential is about  $-45\text{ mV}$  as shown in Figure 11(b).

### Thermophysical properties of nanofluid

The thermo-physical properties of the nanofluid have been calculated using the following equations. The density and specific heat of the nanofluid (Eqs. 1 and 2) are determined using Pak and Cho [48] and Xuan and Roetzel [49].

$$\rho_{nf} = \rho_{bf}(1 - \phi) + \rho_p \phi \quad (1)$$

$$C_{p,nf} = \frac{(\rho_f C_{pf}(1 - \phi)) + \rho_p (C_{pp} \phi)}{\rho_f(1 - \phi) + \rho_p \phi} \quad (2)$$

The effective viscosity of the nanofluid (Eq. 3) is calculated using Brinkman [50] equation.

$$\mu_{nf} = \frac{\mu_{bf}}{(1 - \phi)^{2.5}} \quad (3)$$

Thermal conductivity of the nanofluid (Eq. 4) is given by Hamilton and Crosser [51] model considering shape factor of the nanoparticle

$$k_{nf} = \frac{k_p + (n - 1)k_f - (n - 1)\phi(k_f - k_p)}{k_p + (n - 1)k_f + \phi(k_f - k_p)} k_f \quad (4)$$

Baby and Ramaprabhu relation [52] is implemented for the calculation of thermal conductivity of synthesized GO nanofluid

$$k_{nf} = \frac{k_p(1 - 2\alpha) + 2k_f + 2[k_p(1 - \alpha) - k_f]\phi}{k_p(1 - 2\alpha) + 2k_f - [k_p(1 - \alpha) - k_f]\phi} k_f \quad (5)$$

Here,  $\alpha = \frac{2R_i k_f}{d}$  is the Kapitza constant,  $d$  corresponds to average particle diameter and  $R_i$  is denoted as interfacial thermal resistance.

### Uncertainty analysis

All the experimental data collected are subjected to errors due to the associated uncertainties which are separately listed in Table 3. The uncertainty associated with the individual heat transfer parameters such as power input to cartridge heater, heat extracted by working fluid, heat transfer coefficient, Nusselt number and experimental friction factor quantification is performed using uncertainty propagation [53]. From the analysis the uncertainty involved in power input, heat transfer coefficient, Nusselt number and friction factor are  $\pm 2.2\%$ ,  $\pm 3.5\%$ ,  $\pm 4\%$ , and  $\pm 5.5\%$ , respectively.

### Results and discussion

The thermophysical properties of water and GO nanofluid for different volume fractions are experimentally found. The properties obtained based on experiments

**Table 3.** List of Uncertainty parameters.

Parameters	Uncertainty
Thermal conductivity, $k$ (W/mK)	$\pm 1.0\%$
Density, $\rho$ (kg/m <sup>3</sup> )	$\pm 1.0\%$
Viscosity (cP)	$\pm 0.1\%$
Specific heat (J/kg K)	$\pm 1.0\%$
Voltage, (V)	$\pm 2.0\%$
Current, (A)	$\pm 2.0\%$
Flow rate (L/min)	$\pm 2.2\%$
Temperature of copper sink	$\pm 0.10^\circ\text{C}$
Temperature of heat spreader	$\pm 0.50^\circ\text{C}$
Thermal camera	$\pm 2.0^\circ\text{C}$
Pressure transducer (kPa).	$\pm 3\%$

are then compared with Eqs. (3) and (4) and also with the experimental results provided by Mirzaei and Azimi [54]. Such results are provided in Figures 12 and 13. Figure 12 shows the maximum enhancement in thermal conductivity for GO-0.12% which is 23% more than the base fluid. This augmentation is due to the increased surface area of the GO nanoplatelets and enhanced stability of the nanofluid. The increment in viscosity of GO nanofluid as a function of volume fraction is given in Figure 13. The increment in viscosity by 30% is observed for the GO-0.12% nanofluid than water.

### Temperature distribution on heat spreader

Figures 14–19 show the temperature distribution prevailed in the heat sink and FHU for three different flow rates using water, GO-0.02%, GO-0.07%, and GO-0.12% nanofluid. Additionally, the temperature distribution on different zones of heat spreader is also discussed. Figure 14 shows Infrared-thermal images for heating cycle of the heat sink for a flux of 35 W/cm<sup>2</sup>. Figure 14(a) depicts the increase in temperature of the heat sink up to 50 °C within 25 s. The temperature of the FHU region, which is very near to the channel, increases by 7 °C. In this case, the hotspot is at the right edge of the channel where increase in temperature is more compared to the left side of the channel core. The surrounding temperature of the heat spreader in the PCB increases by 5 °C and a negligible temperature increment is observed at extreme ends of the FHU. But increase in 10 °C was observed after 50 s, shown in Figure 14(b) and the area near the heat sink reaches 60 °C. As noticed, the intensity of the temperature above the processor cores is more than 70 °C. This shows the significance of hotspot penetration over the microchannel heat sink which is generated from the processor core. Figure 15 shows the Infrared photographs of the microchannel module for three time periods using water as working fluid. After the run time of 10 s the temperature prevailed

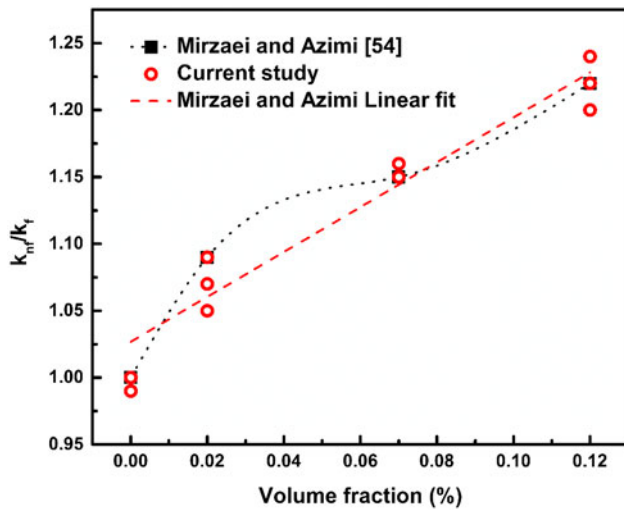


Figure 12. Thermal conductivity of GO/water nanofluid.

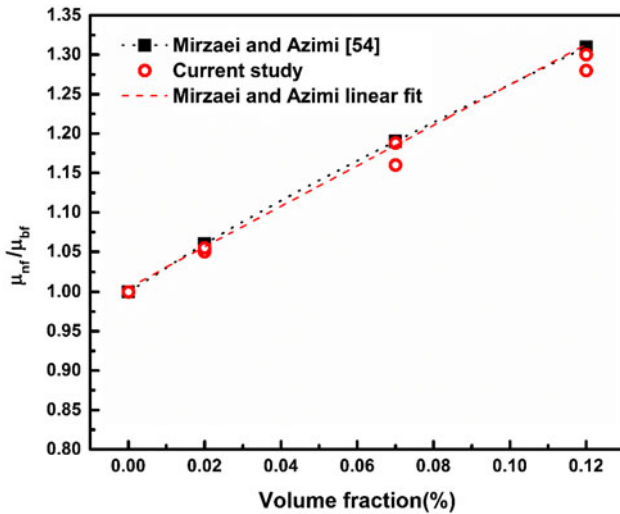


Figure 13. Viscosity of GO/water nanofluid.

in heat sink is about  $33^\circ\text{C}$  and the entire FHU is maintained less than  $30^\circ\text{C}$  which is seen in Figure 15(a). The difference in  $4^\circ\text{C}$  is maintained from inlet to outlet fluids measured from the thermocouples placed within the FHU. The temperatures of the surrounding regions in PCB were minimized to  $40^\circ\text{C}$  from  $65^\circ\text{C}$ . Further progress in time above 20 s there was no much difference in the inlet and the outlet temperatures as shown in Figures 15(b) and (c). Moreover, a steady temperature of  $42^\circ\text{C}$  prevailed throughout the cooling period in area surrounding the heat sink.

Figure 16 depicts the heating and cooling curves for various locations of heat sink and for three different flow rates with water as working fluid. Figure 16(a) shows the temperature distribution for lowest flow rate of  $0.21\text{ L/min}$  as a function of time. On

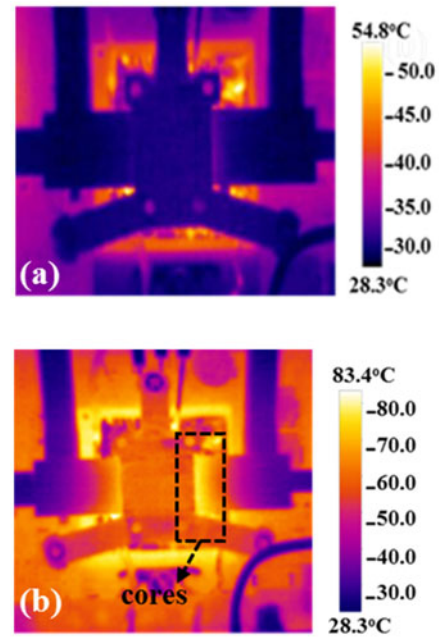
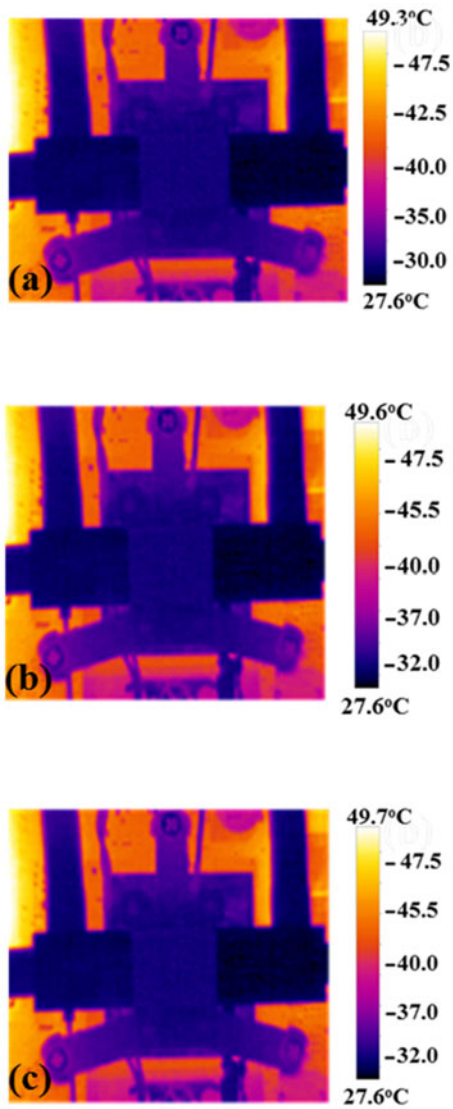


Figure 14. IR photographs of the module at heating at two time periods. (a) 25 s, and (b) 50 s.

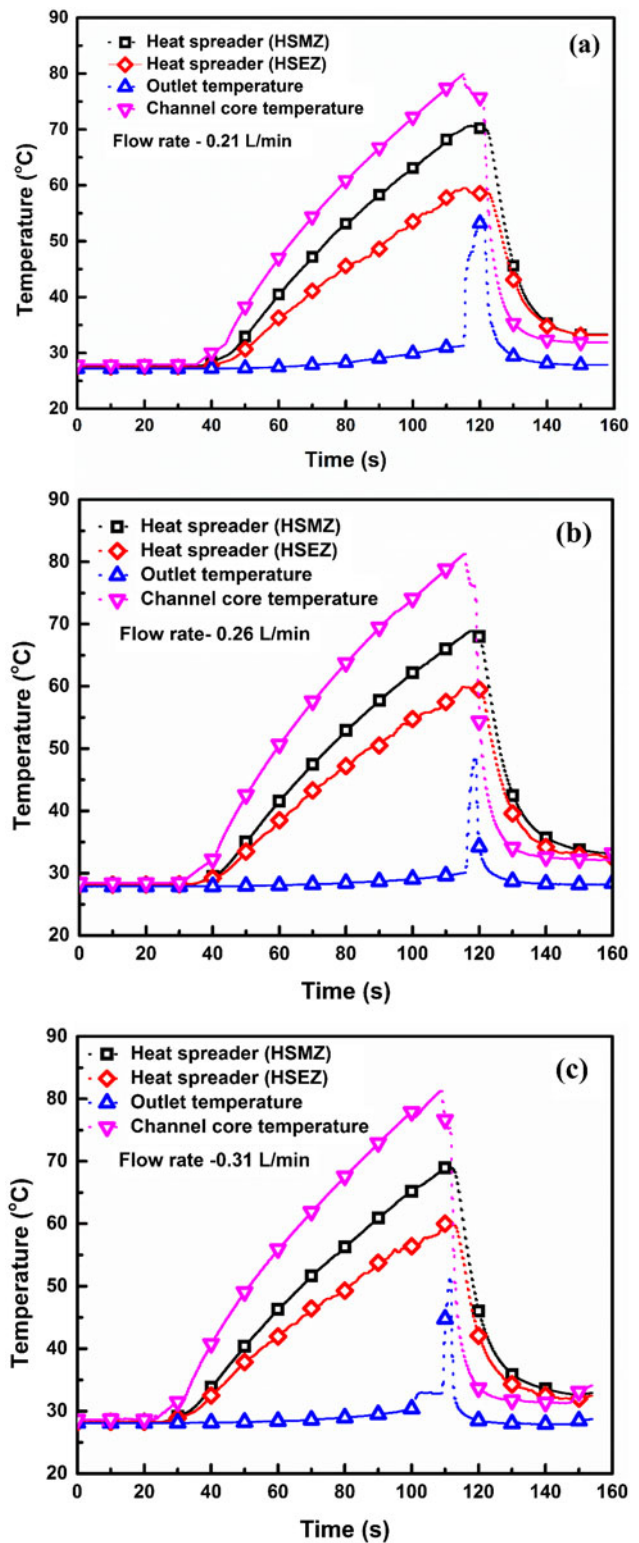
initializing the processor, the maximum temperature reached by microchannel core was  $80^\circ\text{C}$ . The corresponding HSMZ and spreader tip temperatures are  $70^\circ\text{C}$  and  $60^\circ\text{C}$ , respectively. As observed, once the flow is initiated, the outlet temperature increases and temperature of the channel core reduces rapidly. The working fluid takes 5 s to reach the maximum temperature of  $55^\circ\text{C}$  and the HSEZ temperature is still in the range of  $60^\circ\text{C}$ . After the run time of 60 s, the heat sink and core temperature settled down to  $38^\circ\text{C}$ . This instant drop in core temperature is due to the enhanced surface area of parallel microchannel combined with the pulsating flow.

Figure 16(b) shows the temperature distribution for  $0.26\text{ L/min}$ . In this case, the maximum outlet temperature is decreased by  $6^\circ\text{C}$  and all the cooling curves have become comparatively steep. The area under the cooling curve is reduced by 50% and the time taken for the working fluid to attain  $T_f$  is minimized. But still HSMZ maintains the maximum temperature and correspondingly longer time for cooling. The maximum steep curve is developed for higher flow rate of  $0.310\text{ L/min}$  which is shown in Figure 16(c). On close observation, the response time of cooling microchannel core is reduced at increased flow rates. Furthermore, at lower flow rates the effect of fluid diffusion increases and dominates the axial heat conduction in microchannel heat sink which eventually leads to higher temperature in HSMZ. On the other hand, increased flow rates accompanied with nanofluid



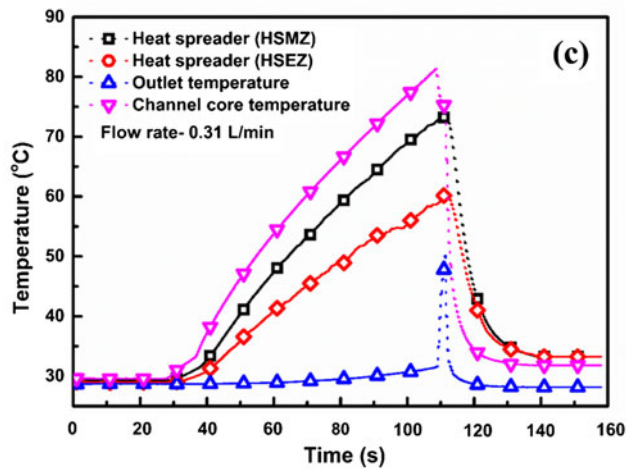
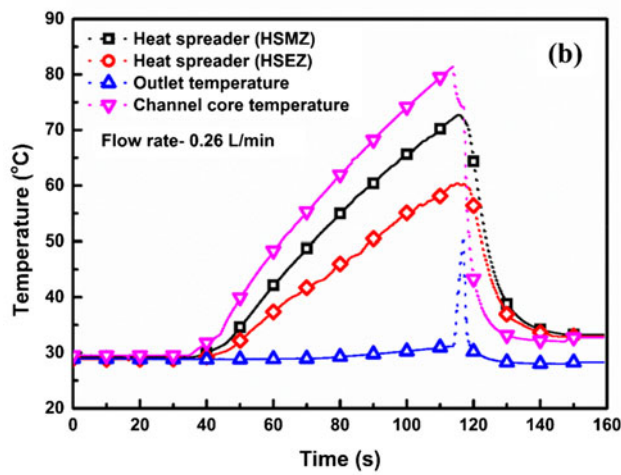
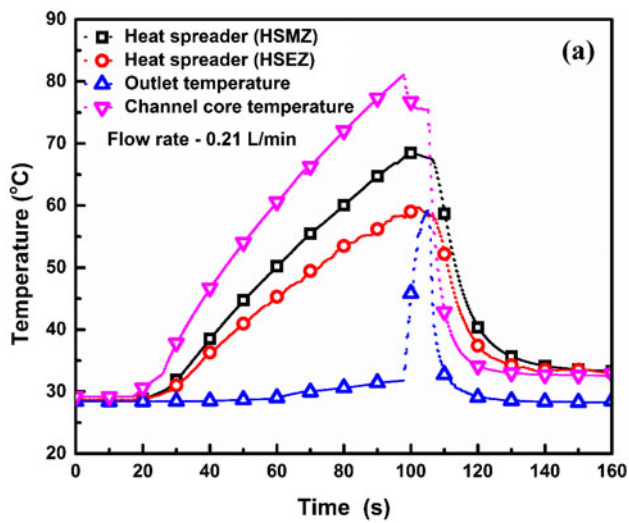
**Figure 15.** IR photographs of the module at progressive cooling at three time periods. (a) 10 s, (b) 20 s, and (c) 30 s.

generates higher temperature due to flow maldistribution in parallel channels. Figure 17 presents the temperature distribution in the heat sink for GO-0.02% nanofluid. At lower flow rate of 0.21 L/min the outlet temperature reaches 60°C which is higher than the outlet temperature developed for water as shown in Figure 17(a). This temperature is equivalent to the temperature noticed in HSEZ of heat spreader in the heat sink. This is majorly due to the increased thermal conductivity of nanofluid combined with reduced flow rate. As observed, the core temperature reduces from 80°C and maintains 75°C for 5 s before it experiences steep decrease in temperature. This clearly shows that there is an effect of bulk fluid conduction in the heat sink especially for nanofluid; but, similar effect was not noticed when water was used as working fluid. With the increased flow rate of 0.26 L/min, there is



**Figure 16.** Temperature distribution with water as working fluid for different flow rates. (a) 0.21 L/min, (b) 0.26 L/min, and (c) 0.31 L/min.

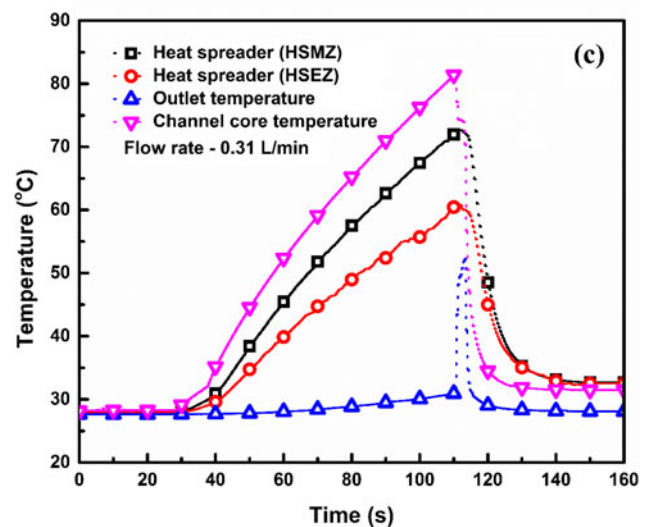
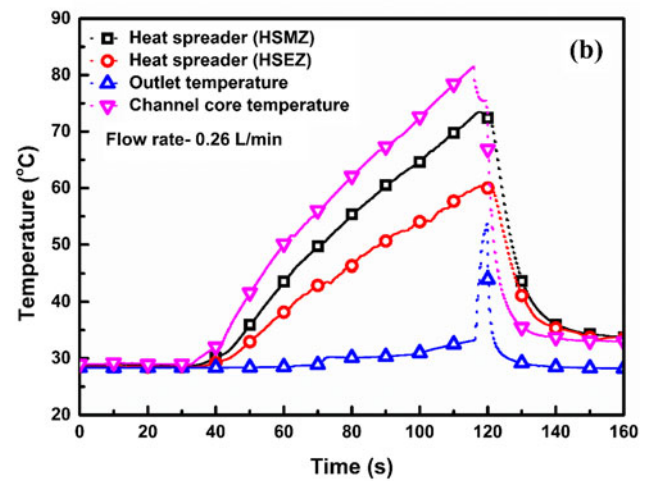
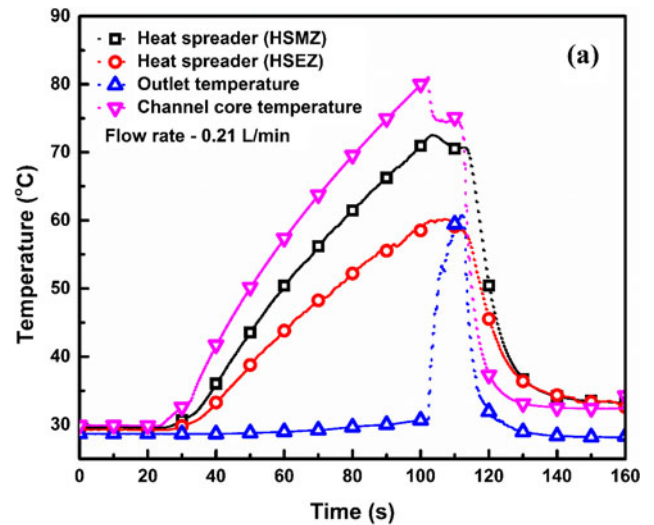
sudden decrease in temperature in all zones of the heat sink as observed in Figure 17(b). The decrease in temperature is steep and the peak of the outlet temperature is comparatively sharp. Further increase in



**Figure 17.** Temperature distribution with GO-0.02% as working fluid for different flow rates. (a) 0.21 L/min, (b) 0.26 L/min, and (c) 0.31 L/min.

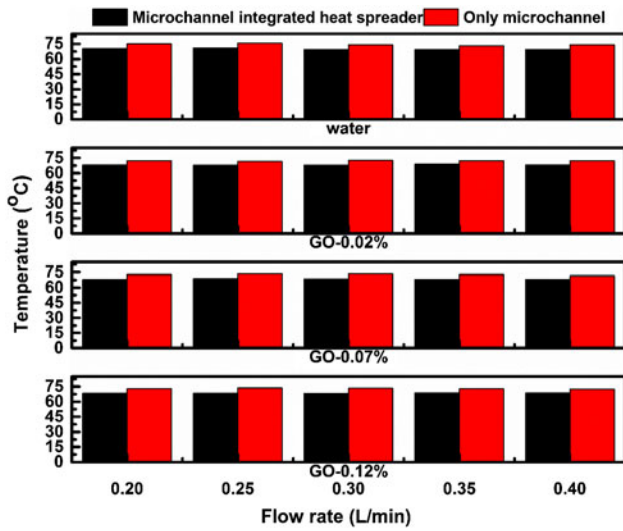
the flow rate reduces the response time and there is no significant effect of fluid bulk diffusion over the heat sink for the flow rate of 0.31 L/min as shown in Figure 17(c).

Figure 18 presents the results for GO-0.12% nano-fluid at different flow rates. At lower flow rate of



**Figure 18.** Temperature distribution with GO-0.12% as working fluid for different flow rates. (a) 0.21 L/min, (b) 0.26 L/min, and (c) 0.31 L/min.

0.21 mL/min the outlet temperature reaches maximum of 62 °C which is higher than the HSEZ temperature as shown in Figure 18(a). Compared to the other two working fluids, the effect of bulk fluid diffusion and



**Figure 19.** Comparison of temperature data for microchannel heat sink and heat spreader integrated microchannel heat sink with different fluids.

axial conduction effects are seen distinctly for the case of GO-0.12% nanofluid. Further increment in flow rate reduces peak outlet temperature by 5–6 °C but not below 50 °C which is shown in Figure 18(b). For 0.31 L/min the cooling in HSMZ and HSEZ is more or less similar to the 0.26 L/min flow rate but temperature drop at core reached maximum refer to Figure 18(c). In all the cases the temperature of HSMZ and HSEZ is about 3–4 °C more than the core temperature.

From the above observations the axial conduction effects combined with flow maldistribution in parallel microchannel develop higher temperature at outlet region of the micro channels. This effect further intensifies for high thermal conductivity nanofluid at lower flow rates. The core temperature reduces by 6 °C due to the increased thermal conductivity but at the same time the heat sink is subjected to fluid diffusion based conduction effects. In the case of higher flow rates for all subjected fluids the channel core and HSMZ temperatures have less marginal gap for the first time. Over all the increase in HSMZ temperature is majorly due to the migrated temperature from the sink core.

The comparison of temperature between microchannel heat sink and microchannel integrated heat spreader module with different fluids is shown in Figure 19. The temperature variations are taken using thermocouple  $T_3$  for both heat sinks, which represent the location of flow maldistribution hotspot region. The microchannel heat sink shows higher temperature than the microchannel with spreader for all the flow rates and working fluids. More than 10% decrease in

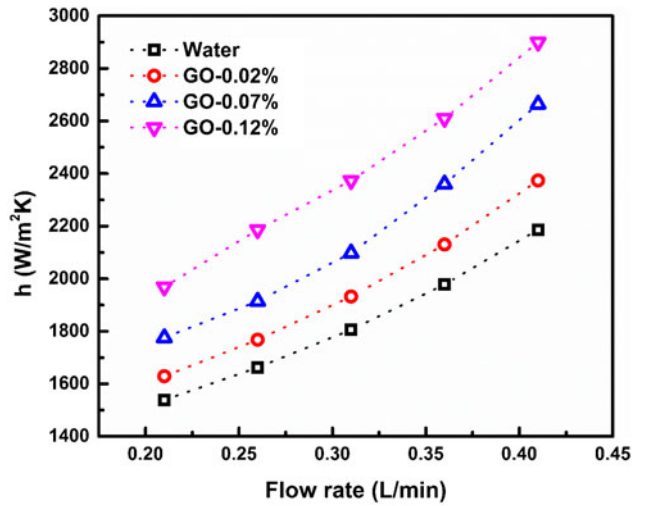


**Figure 20.** Heat transfer coefficient as a function of flow rate for different volume fractions.

temperature was observed by implementing heat spreader. For all the flow rates and working fluids considered, an average increase of 7 °C is observed for the case of only microchannel heat sink module. Apparently, for microchannel heat sink case the maldistribution flow induced hotspot accumulates near the exit of the microchannel. Subsequently, there is increase in temperature  $T_3$  not only due to maldistribution but also the effect of axial conduction. As noticed, when the heat spreader is integrated with the microchannel heat sink the temperature  $T_3$  reduces significantly.

### Heat transfer studies

The experimental observations were made for five different flows rates ranging from 0.21 to 0.45 L/min. The local heat transfer coefficient is obtained from the following equation

$$h_x = q''(T_w - T_f) \quad (6)$$

where  $q''$  is the heat flux subjected to the walls of the electronic chip.  $T_w$  is the temperature measured along the length of the channel.  $T_f$  is defined as the average fluid temperature. Local Nusselt number in the study is defined as

$$Nu_x = h_x D_h / k_f \quad (7)$$

where  $D_h$  is the hydraulic diameter of the microchannel which is given as  $D_h = 2ab/a + b$ ,  $a$  and  $b$  are the corresponding length and breadth of the microchannel. The average Nusselt number for the present study is reported by calculating the average heat transfer coefficient along the channel length which is given by

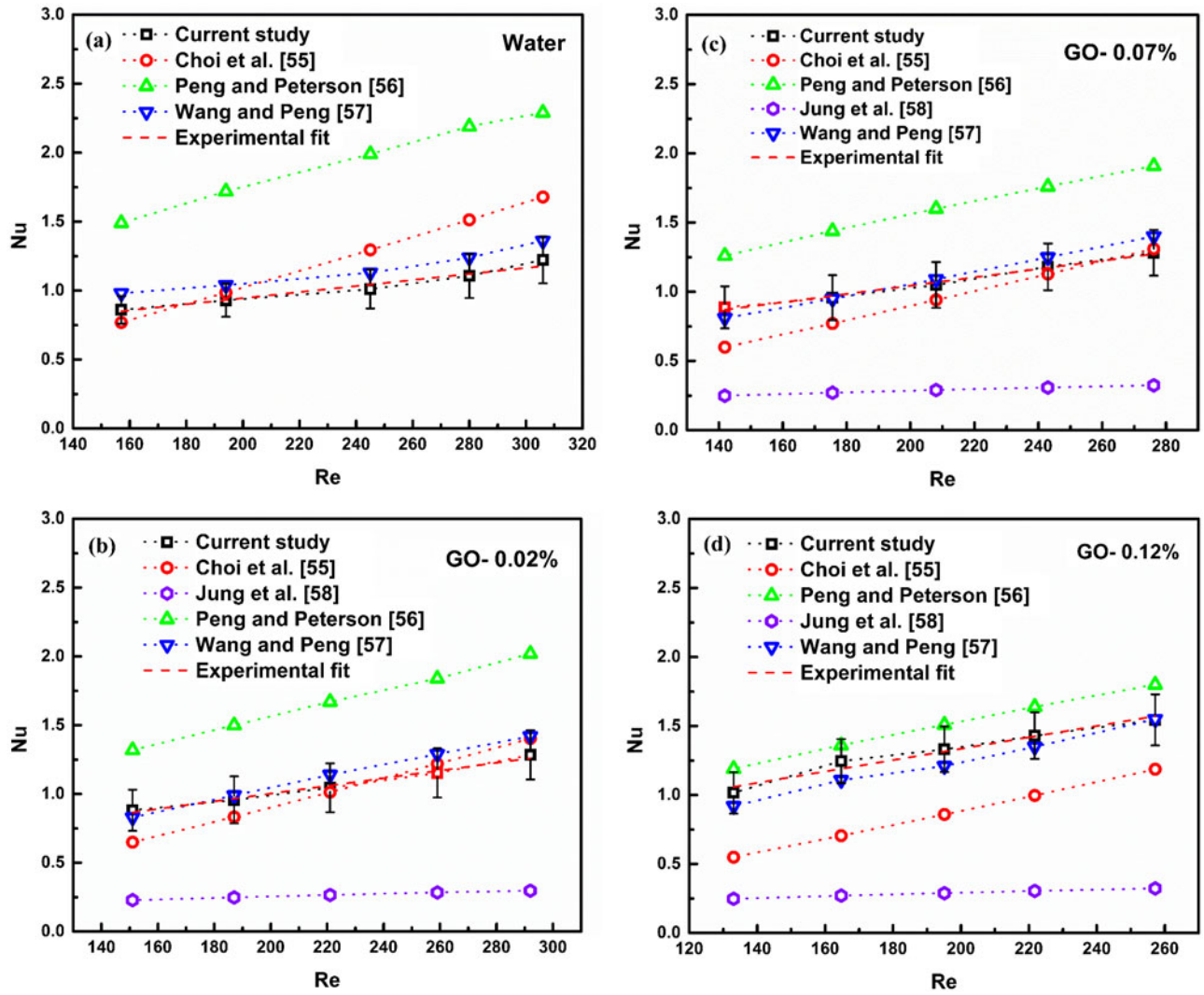


Figure 21. Nusselt number variation as the function of Reynolds number.

$$h_{\text{avg}} = \frac{\int_0^L h_x(T_w - T_f)dA}{A(\bar{T}_w - \bar{T}_f)} \quad (8)$$

$$Nu_{\text{avg}} = \frac{1}{L} \int_0^L Nu_x dx \quad (9)$$

Figure 20 shows the increase in heat transfer coefficient with respect to GO/water nanofluid for different volume fractions and increased flow rates. It can be seen that the heat transfer coefficient calculated using Eq. (6) increases with increasing flow rate. Similarly, higher volume fraction of nanoparticles results in enhancement of heat transfer coefficient. The maximum heat transfer coefficient was achieved for volume fraction of GO-0.12%.

Figure 21 depicts the experimental comparison of Nusselt number for three different nanofluids for the Reynolds number ranging from 100 to 320. It was observed that the Nusselt number was found to be

maximum at the higher flow rates. This trend was also seen in other three GO nanofluids. The maximum Nusselt number was obtained for GO-0.12% nanofluid which is 77% higher than water. Additionally, the Nusselt number obtained using the present experimental data is compared with the existing benchmark correlations proposed by Choi *et al.* [55], Peng and Peterson [56], Wang and Peng [57], and Jung *et al.* [58].

Choi *et al.* [55] presented a correlation for the Nusselt number for micro tubes and water as working fluid for  $Re < 2200$  and is given in Eq. (10)

$$Nu = 0.000972Re^{1.17}Pr^{1/3} \quad (10)$$

where  $Re$  is the Reynolds number calculated as  $\rho_f uD/\mu_f$  and  $Pr$  is the Prandtl number given as  $C_{p_f} \mu_f/k_f$ . Peng and Peterson [56] proposed a correlation for Nusselt number for the Reynolds number ranging between 200 and 4,000 and  $Pr = 1.69$ . Their



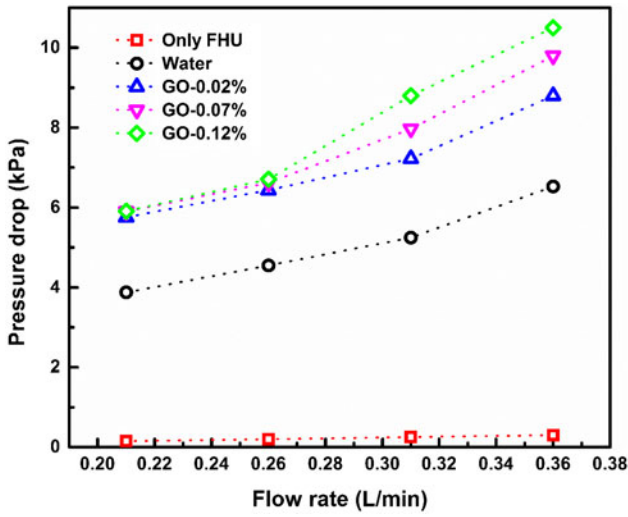


Figure 22. Pressure drop as a function of flow rate for different fluids.

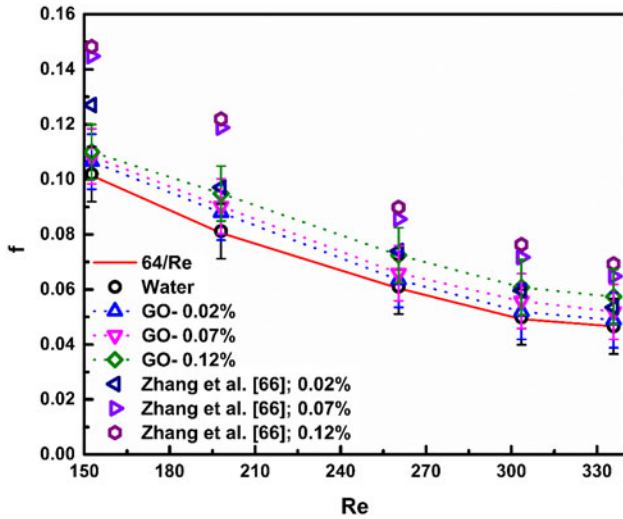


Figure 23. Friction factor as a function of Reynolds number for different fluids.

proposed correlation has a maximum deviation of  $\pm 30\%$ , the correlation is as follows

$$Nu = 0.1165(D_h/W_c)^{0.81}(H/W)^{-0.79}Re^{0.62}Pr^{1/3} \quad (11)$$

Wang and Peng [57] presented Nusselt number correlation on rectangular channels for Reynolds number ( $70 < Re < 1500$ ) for  $Pr$  ranging between 2.69 and 7.56. Eq. (12) represents a correlation developed from experimental data for all the tested channels with a maximum deviation of  $\pm 25\%$ .

$$Nu = 0.0080Re^{4/5}Pr^{1/3} \quad (12)$$

Jung *et al.* [58] proposed a modified form of Dittus-Boelter equation for microchannels which includes a volume fraction for the nanoparticle for a range of  $Pr$  ( $0.6 < Pr < 160$ ) and Reynolds number ( $0 < Re < 350$ ).

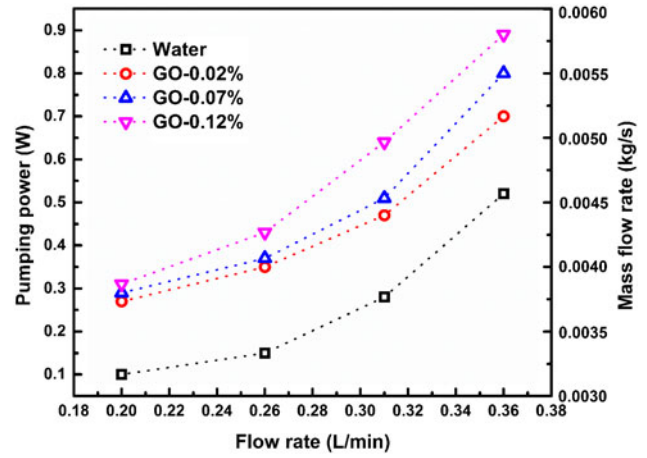


Figure 24. Pumping power as a function of flow rate for different fluids.

$$Nu = 0.014\phi^{0.095}Re^{0.4}Pr^{0.6} \quad (13)$$

Figure 21(a) depicts the variation of experimental Nusselt number for increased Reynolds number with water as working fluid in the rectangular microchannel. The Nusselt number is calculated using Eq. (9) for which the required wall temperature and bulk fluid for the applied heat flux are acquired from thermocouple data. As seen, in Figure 21(a) the experimental results having a deviation of  $\pm 2\%$  is compared with correlation developed proposed by Choi *et al.* [55] and Wang and Peng [57] for water and found to have a deviation of 6%. But a maximum deviation of 30% was observed for Peng and Peterson [56] and the predicted Nusselt number was higher than that of experimental results. Similar discrepancies were noted for the results presented by Qu *et al.* [59] and Peng *et al.* [60]. Peng and Peterson [56] suggested a correlation that takes in to account the height and width of microchannel which may be one of the reasons for the deviation. Since the aspect ratio of the channel considerably affects the thermal and flow characteristics [61,62]; the current study has high temperature core at entrance of the microchannel, that results in temperature difference at inlet and outlet sections of the microchannel. The thermal gradient in the microchannel heat sink resulted by hotspot could conceivably be reduced with the use of nanofluid. Nevertheless, use of nanofluid in parallel microchannel undergoes flow maldistribution and axial conduction effects there by increasing the temperature of the outlet section of the microchannel. But comparatively the thermal gradient developed by flow maldistribution induced hotspots is relatively lower than the hotspot cores.

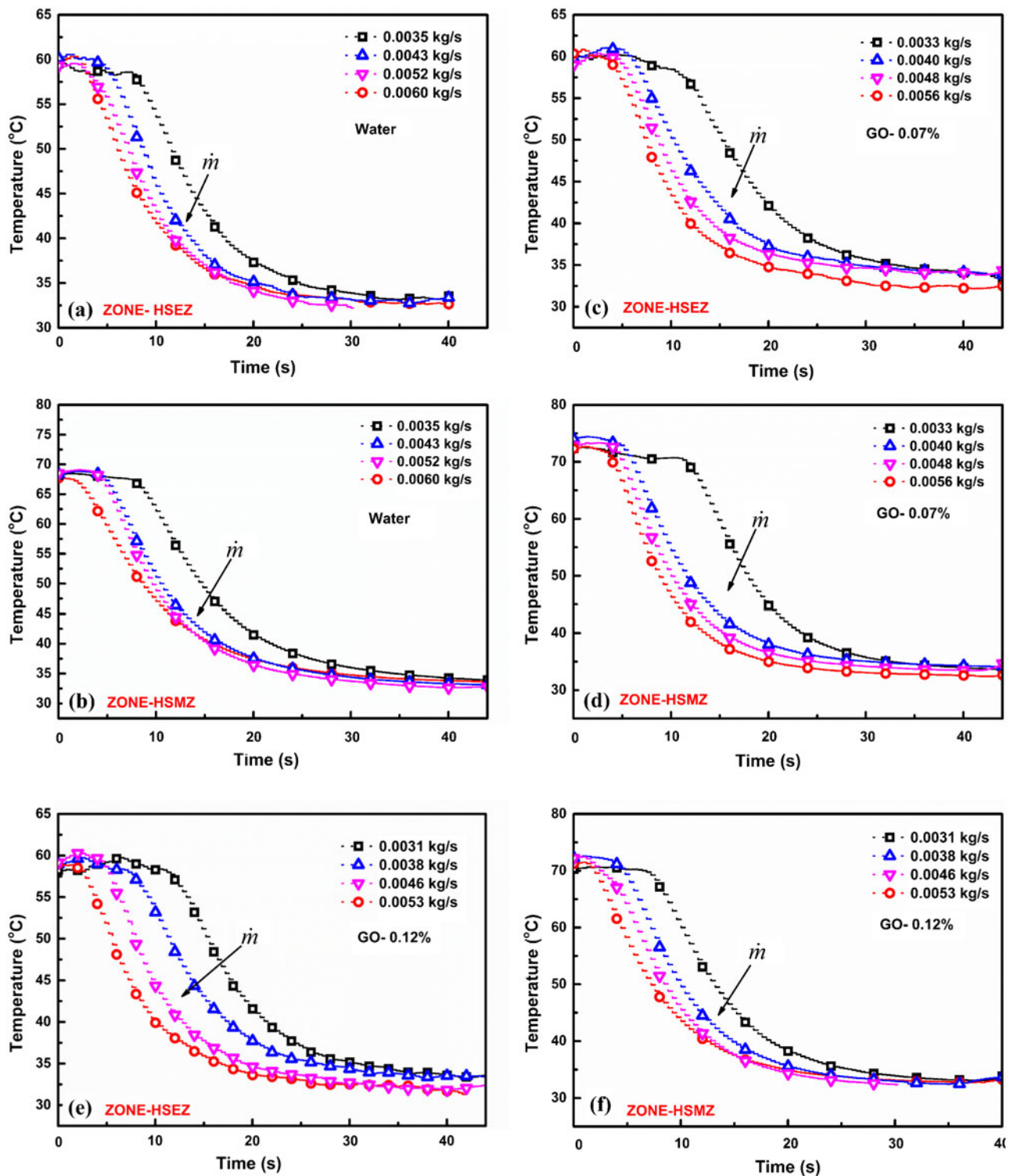


Figure 25. Heat spreader temperature distribution for different flow rates. (Direction of arrow indicates the increase in mass flow rate).

In order to show the enhancement of GO nanofluid, the experimental results were demonstrated with other established Nusselt number correlation. Moreover, Nusselt number correlation for nanoplatelets based nanofluid using microchannel are not yet established clearly. On other hand, the performance of

microchannels with very low  $\nu_f$  nanofluid for heat transfer augmentation has been focused much by the researchers recent times. As a result, the GO nanofluid used in the present study is added with nanoparticle  $\nu_f$  less than 1% and the correlations available for pure fluid are then used to study the effect of GO

nanoparticle. Figure 21(b) shows the Nusselt number for GO-0.02% as a function of Reynolds number. The results demonstrated that GO-0.02% nanofluid provided improved heat transfer performance than water. The experimental results evidently show the influence of lower vf of GO-0.02% nanofluid in augmentation of Nusselt number. However, the influence of nanoparticle is not substantially noticed at increased vf of GO-0.07% as shown in Figure 21(c). The reason might be attributed to the increased conduction effects of the heat sink due to the increased bulk fluid temperature for higher thermal conductivity nanofluid at lower Reynolds number. This increases the thermal gradient of microchannel heat sink, as discussed in temperature study section, refer to Figures 16–18. Furthermore, increase in vf to GO-0.12% reduced the deviation from the predictions of Peng and Peterson [56] as shown in Figure 21(d).

From these observations, it is clear that the improved performance of microchannel heat transfer at higher Reynolds number is predominantly due to the augmented thermal conductivity of GO nanofluid and enhanced stability of the GO nanoparticles in the base fluid. Additionally, the shape factor of the GO nanoparticles enhances the contact of nanoparticle with base fluid [63]. This progressively increases the particle collision and escalates heat transfer mechanisms according to Brownian motion, Thermophoresis and Ballistic transport [64]. The above mentioned GO nanoparticle characteristics and mechanisms eventually intensifies the thermal energy transport owing to diffusion and thereby increasing the bulk cooling fluid temperature. Concurrently, the increased GO volume fraction contributes higher particle interaction with microchannel wall with increased momentum which results in effective thermal transport. It was observed that the effect of Reynolds number is highly sensitive for higher volume fraction nanofluid. As observed, for lower Reynolds number the bulk fluid temperature of the nanofluid is higher and increases the heat sink temperature with highly stable and directional temperature gradients. This increase in bulk fluid conduction in heat sink was predominant at lower Reynolds number and the effects are profoundly seen for higher vf nanofluid and similar effect was observed by Ebrahimi *et al.* [65].

### Friction factor

Figure 22 shows the increase in pressure drop as a function of flow rate for different working fluids. It is

clearly seen that the addition of GO nanoparticles linearly increases the pressure drop and amplifies even further at higher flow rate. A maximum pressure drop of 6 kPa was developed for water at 0.36 L/min. For the same flow rate GO-0.12% nanofluid developed pressure drop of 10 kPa. On comparison with water the use of nanofluid in microchannel heat sink augments the pressure drop by 45% for GO-0.02% and 60% in the case of GO-0.12%.

Moreover, the difference in pressure drop among GO nanofluid is minimal at lower flow rates but a very low concentration GO-0.02% nanofluid generates significant pressure drop than water. It is evident that at lower flow rate the nanoplatelets are marginally assisted by gravity and at higher flow rate channel surface effects and entrance effects amplifies the pressure drop to a maximum limit.

The experimentally measured pressure drop across the microchannel in FHU is used to calculate experimental friction factor by the following equation given in Eq. (14)

$$f = \frac{\Delta P D_h}{1/2 \rho \bar{u}^2 L} \quad (14)$$

In Figure 23 the experimental friction factor is compared with the theoretical friction factor predicted using Hagen- poiseuille equation given by Eq. (15) as a function of Reynolds number ranging from 150 to 350 with error less than  $\pm 2\%$ .

$$f = \frac{64}{Re} \quad (15)$$

A considerable agreement with a deviation of 3% was found between the theoretical and experimental friction factors. For low volume fraction of 0.02%, typical friction factor result was observed, in which the friction factor decreases as Reynolds number increases. In the case of higher volume concentration of GO-0.12%, the friction factor increased by 20% due to the increased viscosity developed for higher mass fraction; consequently, the use of lower volume fraction of 0.02% resulted in increase of friction factor by 6% than water. This certainly shows that even for very low volume fraction of GO nanoplatelets a considerable increase in friction factor is unavoidable. This penalty in friction factor is highly attributed to substantial increment in surface area of GO nanoplatelets based nanofluids.

Additionally, the experimental results were compared with the friction factor correlations obtained by Zhang *et al.* [66]. The error developed by using 0.02, 0.07, and 0.12 vf% in this correlation for examined Reynolds number were 34%, 41%, and 48%,

respectively. As observed in Figure 23, the experimental results when compared with Zhang *et al.* [66] resulted in higher friction factor than the current study. But still at higher Reynolds number the predicted friction factor of GO nanofluid agrees well with the experimental results. This is due to the proposed correlation that was investigated for a Reynolds number range of 600–2,000. Moreover, they used circular cross section with comparatively denser  $\text{Al}_2\text{O}_3$  nanofluid.

Figure 24 shows the results of pumping power, refer to Eq. (16), with respect to the flow rate for water and GO nanoplatelets based nanofluid.

$$P_p = Q \cdot \Delta P = \frac{\dot{m} \Delta P}{\rho} \quad (16)$$

Here,  $Q$  is volumetric flow rate and  $\Delta P$  is experimentally obtained pressure difference from microchannels. As noticed, the pumping power increases as the flow rate increases for all the fluids. Furthermore, the increase in particle concentration additionally increases the pumping power. This implies pumping power majorly relies on factors such as flow rate and volume fraction of nanofluid. The maximum pumping power of 0.87 W was generated by GO-0.12% which is 74% higher than water for the same flow rate of 0.36 L/min. But the deviation of pumping power between GO-0.02% and GO-0.12% is comparatively lower by about 25%.

### Hotspot migration

The use of the heat spreader with the microchannel allows for the study of thermal energy migration from the channel core to various regions of the large surface area heat spreader under different flow rates. Depending on the flow rates the movement of temperature distribution in heat spreader is parallel to the flow and along the direction of the fluid. Thus the heat spreader facilitates to extract high density thermal loads developed by multicore processor. This migration of higher temperature in heat spreader is qualitatively captured by experimentation which is shown in Figures 25(a–f). Figure 25(a) shows the temperature in HSEZ for varying mass flow rate of 0.0035 to 0.0060 kg/s for water with a constant heat flux of  $35 \text{ W/cm}^2$ . For the case of mass flow rate 0.0035 kg/s, the temperature at HSEZ slightly decreased by  $2^\circ\text{C}$  and maintains  $58^\circ\text{C}$  till 10 s and then the temperature of HSEZ decreases rapidly to  $35^\circ\text{C}$ . This is majorly attributed to the lower flow rate, but the effect of cooling wave is experienced in HSEZ due to the initial

decrease in temperature of  $2^\circ\text{C}$ . In the case of 0.0043 kg/s, there is no effect of initial decrease in temperature at HSEZ, but rapid decrease in temperature is noticed within 5 s. In this consideration, with the increased mass flow rate the effect of thermal migration is reduced by 50% and relative cooling performance of the heat sink is doubled. For the cases of 0.0052 and 0.0060 kg/s similar decrease in HSEZ temperature is observed. The results of temperature for HSMZ are shown in Figure 25(b). The effect of initial decrease in temperature in HSMZ is not observed and the temperature decrement is comparatively more gradual than HSEZ. The decrease in temperature for higher mass flow rates developed identical curves after 10 s, but did not reduce the spreader temperature less than  $35^\circ\text{C}$ . These combined effects in HSEZ and HSMZ reveal that once the flow is initiated within the heat spreader there exhibits a decrease in transfer of thermal energy from the heat sink core. Note that at this point the cooling wave has propagated throughout the heat spreader except HSMZ, since it is in the vicinity of high temperature region generated by flow maldistribution induced hotspot at the exit of the microchannel.

Figures 25(c) and (d) represent the temperature distribution for GO-0.07% nanofluid with different mass flow rates. For the lower mass flow rate of 0.0033 kg/s the temperature of HSEZ decreased with comparatively higher time period than HSEZ of water as shown in Figure 25(c). The explanation for this higher time period is due to the increased thermal conductivity of the GO-0.07% nanofluid. This in turn causes the nanofluid to carry more heat towards the HSEZ region. More appropriately the conduction effects in the heat sink influenced by bulk fluid diffusion potentially ceases the drastic transmit of cooling to HSEZ region. As demonstrated, the decrease in HSEZ temperature is very drastic for increased mass flow rate of 0.0040 kg/s with the reduced time period of 30%. On other hand, the corresponding differences in time period between mass flow rates of 0.0048 and 0.0056 kg/s are comparatively lower. Due to the combined impact of increased mass flow rate and thermal conductivity, the temperature of the HSEZ region reaches  $33^\circ\text{C}$  which is more or less near to room temperature. Figure 25(d) shows the temperature decrement at HSMZ as a function of time for different mass flow rates. It is observed that the maximum temperature of HSMZ region increases to  $76^\circ\text{C}$  and is higher compared to water. Most importantly, the temperatures of the heat spreader are at two different temperatures with the difference of  $16^\circ\text{C}$  at the same

time period. This large increment in HSMZ temperature is attributed to increased thermal conductivity and lower flow rate which increases the outlet fluid temperature more than  $60^{\circ}\text{C}$  as seen in temperature study section. Besides the increment in HSMZ temperature, the higher thermal energy migration from the microchannel to the heat spreader has increased by using higher volume fraction nanofluid. Moreover, more stable temperature distribution in heat spreader has been developed by GO-0.12% nanofluid presented in Figure 25(e). As noticed before in GO-0.07%, the temperature of HSEZ increased gradually for more than 10 s and then it reduces. However, no significant temperature stability is seen in HSMZ as shown in Figure 25(f). Since the HSMZ is near the microchannel outlet, the temperature of  $70^{\circ}\text{C}$  is maintained nearly 10 s at lower mass flow rate of  $0.0031\text{ kg/s}$  which was noticed only for GO nanofluid. But once the flow rate is increased the temperature of HSMZ drops drastically similar to all the other working fluids. Moreover, for all the fluids there exists an increase in temperature of  $2^{\circ}\text{C}$  in HSMZ even though the heat sink is subjected to cooling. This increase is due to thermal migration from outlet region of the sink to HSMZ.

## Conclusions

Experimental investigations were performed on the rectangular microchannel accompanied with heat spreader for various flow rates using water and GO with three different volume fractions (GO-0.02%, GO-0.07%, and GO-0.12%) as working fluid. For a constant heat flux of  $35\text{ W/cm}^2$ , the heat removal rate of GO-0.12% nanofluid was found superior to pure fluid, GO-0.02% and GO-0.07%. The important key findings are

- Heat spreader effectively operates at a lower flow rate of  $0.21\text{--}0.30\text{ L/min}$ , beyond that the presence of heat spreader is compromised.
- The Nusselt number was found to increase by 77% with the use of GO-0.12% nanofluid.
- The surrounding temperature, prevailed near to the heat sink, drops from  $60^{\circ}\text{C}$  to  $42^{\circ}\text{C}$  due to the supply of high thermal conductivity fluid in microchannel.
- Experimental characterization demonstrates that the contribution of very low concentration (GO-0.02 vf%) can alter the hydrodynamic and heat transfer phenomena.

- It has been found that the GO nanofluid as working fluid provides steady cooling and can effectively be suitable for handling high flux density components without compromising packaging for highly compact electronic devices.
- Due to low pumping cost and miniaturization of electronic equipment, the micro heat sink presented in this work provides a better and profitable solution as a compact electronic cooling device.

## Notes on contributors



**Ganesan Narendran** graduated in Mechanical Engineering from Anna University, Tiruchy (2012). He pursued his Masters at Indian Institute of Information Technology Design and Manufacturing, Kancheepuram (2014). Currently, he is a research scholar in the Department of Mechanical Engineering at National Institute of Technology Karnataka Surathkal. His research activity focuses on experimental and numerical investigation in microchannel based compact electronic cooling devices for densely packed electronic systems.



**Nagarajan Gnanasekaran** is an Assistant Professor in the Department of Mechanical Engineering at the National Institute of Technology Karnataka, India. He graduated in Mechanical Engineering (2002) from Bharathidasan University and obtained his Master of Engineering in Thermal Engineering (2006) from Government College of Technology and Ph.D. from Indian Institute of Technology Madras (2012), Chennai under the supervision of Prof. C. Balaji. His research interests include computational inverse problems, stochastic modeling techniques, experimental and numerical heat transfer and hybrid optimization, fluid flow and heat transfer in porous media and micro channel heat transfer.



**Dharmaraj Arumuga Perumal** received B.E. degree in Mechanical Engineering from Manonmaniam Sundaranar University, and M.E. degree in Thermal Engineering from Government College of Technology, Coimbatore. He received his Ph.D. degree in the field of lattice Boltzmann method for fluid flows from the Department of Mechanical Engineering, Indian Institute of Technology, Guwahati. He is currently working as Assistant Professor in the Dept. of Mechanical Engineering, National Institute of Technology Karnataka, Surathkal, Mangalore, India. His current research interests are predominantly focused on the simulation of flows using lattice Boltzmann method and micro- and nanofluidics.

## References

- G. E. Moore, "Cramming more components onto integrated circuits," *Proc. IEEE*, vol. 86, no. 1, pp. 82–85, 1998. DOI: [10.1109/JPROC.1998.658762](https://doi.org/10.1109/JPROC.1998.658762).
- M. Gad-Ed-Hak, "The fluid mechanics of microdevices- the freeman scholar lecture," *J. Fluid Eng.*, vol. 121, no.1, pp. 5–33, 1999.
- D. B. Tuckerman, and R. F. W. Pease, "High-performance heat sinking for VLSI," *IEEE Electron Device Lett.*, vol. 2, no. 5, pp. 126–129, 1981. DOI: [10.1109/EDL.1981.25367](https://doi.org/10.1109/EDL.1981.25367).
- A. Abdollahi, R. N. Sharma, H. A. Mohammed, and A. Vatani, "Heat transfer and flow analysis of Al<sub>2</sub>O<sub>3</sub>-water nanofluids in interrupted microchannel heat sink with ellipse and diamond ribs in the transverse microchambers," *Heat Transf. Eng.*, vol. 39, no. 16, pp. 1461–1469, 2018.
- O. O. Adewami, T. Bello-Ochende, and J. P. Meyer, "Numerical investigation into the thermal performance of single microchannels with varying axial length and different shaped of micropin- fin inserts," *Heat Transf. Eng.*, vol. 38, no. 13, pp. 1157–1170, 2017. DOI: [10.1080/01457632.2016.1239927](https://doi.org/10.1080/01457632.2016.1239927).
- S. R. Reddy *et al.*, "Multi objective optimization for cooling of high heat flux electronics with a hot spot," *Heat Transf. Eng.*, vol. 38, no. 14–15, pp. 1235–1246, 2017. DOI: [10.1080/01457632.2016.1242953](https://doi.org/10.1080/01457632.2016.1242953).
- H. V. Moradi, and J. M. Floryan, "Maximization of heat transfer across micro-channels," *Int. J. Heat Mass Transf.*, vol. 66, pp. 517–530, 2013. DOI: [10.1016/j.ijheatmasstransfer.2013.07.059](https://doi.org/10.1016/j.ijheatmasstransfer.2013.07.059).
- A. Sakanova, C. C. Keian, and J. Zhao, "Performance improvements of microchannel heat sink using wavy channel and nanofluids," *Int. J. Heat Mass Transf.*, vol. 89, pp. 59–74, 2015. DOI: [10.1016/j.ijheatmasstransfer.2015.05.033](https://doi.org/10.1016/j.ijheatmasstransfer.2015.05.033).
- J. P. McHale, and S. V. Garimella, "Heat transfer in trapezoidal microchannels of various aspect ratios," *Int. J. Heat Mass Transf.*, vol. 53, no. 1–3, pp. 365–375, 2010. DOI: [10.1016/j.ijheatmasstransfer.2009.09.020](https://doi.org/10.1016/j.ijheatmasstransfer.2009.09.020).
- H. Y. Wu, and P. Cheng, "Friction factors in smooth trapezoidal silicon microchannels with different aspect ratios," *Int. J. Heat Mass Transf.*, vol. 46, no. 14, pp. 2519–2525, 2003. DOI: [10.1016/S0017-9310\(03\)00106-6](https://doi.org/10.1016/S0017-9310(03)00106-6).
- V. Glazar, B. Frankovic, and A. Trp, "Experimental and numerical study of the compact heat exchanger with different microchannel shapes," *Int. J. Refrigeration*, vol. 51, pp. 144–153, 2015. DOI: [10.1016/j.ijrefrig.2014.06.017](https://doi.org/10.1016/j.ijrefrig.2014.06.017).
- S. U. S. Choi, "Enhancing thermal conductivity of fluids with nanoparticles," in *Developments Applications of Non-Newtonian Flows*, vol. 66, D. A. Signer and H. P. Wang, Eds. New York: ASME, 1995, pp. 99–105.
- J. Koo, and C. Kleinstreuer, "Laminar nanofluid flow in microheat-sinks," *Int. J. Heat Mass Transf.*, vol. 48, no. 13, pp. 2652–2661, 2005. DOI: [10.1016/j.ijheatmasstransfer.2005.01.029](https://doi.org/10.1016/j.ijheatmasstransfer.2005.01.029).
- P. Bhattacharya, A. N. Samanta, and S. Chakraborty, "Numerical study of conjugate heat transfer in rectangular microchannel heat sink with Al<sub>2</sub>O<sub>3</sub>/H<sub>2</sub>O nanofluid," *Heat Mass Transf.*, vol. 45, no. 10, pp. 1323–1333, 2009. DOI: [10.1007/s00231-009-0510-0](https://doi.org/10.1007/s00231-009-0510-0).
- M. Azimi, and A. Mozaffari, "Heat transfer analysis of unsteady graphene oxide nanofluid flow using a fuzzy identifier evolved by genetically encoded mutable smart bee algorithm," *Eng. Sci. Technol. Int. J.*, vol. 18, no. 1, pp. 106–123, 2015. DOI: [10.1016/j.jestech.2014.10.002](https://doi.org/10.1016/j.jestech.2014.10.002).
- W. Yu, H. Xie, and D. Bao, "Enhanced thermal conductivities of nanofluids containing graphene oxide nanosheets," *Nanotechnology*, vol. 21, no. 5, pp. 055705, 2010. DOI: [10.1088/0957-4484/21/5/055705](https://doi.org/10.1088/0957-4484/21/5/055705).
- M. N. M. Zubir *et al.*, "Highly dispersed reduced graphene oxide and its hybrid complexes as effective additives for improving thermophysical property of heat transfer fluid," *Int. J. Heat Mass Transf.*, vol. 87, pp. 284–294, 2015.
- V. M. Siva, A. Pattamatta, and S. K. Das, "Effect of flow maldistribution on the thermal performance of parallel microchannel cooling systems," *Int. J. Heat Mass Transf.*, vol. 73, pp. 424–428, 2014. DOI: [10.1016/j.ijheatmasstransfer.2014.02.017](https://doi.org/10.1016/j.ijheatmasstransfer.2014.02.017).
- G. Kumaraguruparan, R. M. Kumaran, T. Sornakumar, and T. Sundararajan, "A numerical and experimental investigation of flow maldistribution in a micro-channel heat sink," *Int. Commun. Heat Mass Transf.*, vol. 38, no. 10, pp. 1349–1353, 2011. DOI: [10.1016/j.icheatmasstransfer.2011.08.020](https://doi.org/10.1016/j.icheatmasstransfer.2011.08.020).
- R. M. Kumaran, G. Kumaraguruparan, and T. Sornakumar, "Experimental and numerical studies of header design and inlet/outlet configurations on flow mal-distribution in parallel micro-channels," *Appl. Therm. Eng.*, vol. 58, no. 1–2, pp. 205–216, 2013. DOI: [10.1016/j.applthermaleng.2013.04.026](https://doi.org/10.1016/j.applthermaleng.2013.04.026).
- S. A. Solovitz, "Analysis of parallel microchannels for flow control and hot spot cooling," *J. Thermal Sci. Eng. Appl.*, vol. 5, no. 4, pp. 041007, 2013. DOI: [10.1115/1.4024021](https://doi.org/10.1115/1.4024021).
- L. S. Maganti, P. Dhar, T. Sundararajan, and S. K. Das, "Heat spreader with parallel microchannel configurations employing nanofluids for near-active cooling of MEMS," *Int. J. Heat Mass Transf.*, vol. 111, pp. 570–581, 2017. DOI: [10.1016/j.ijheatmasstransfer.2017.04.032](https://doi.org/10.1016/j.ijheatmasstransfer.2017.04.032).
- L. S. Maganti, P. Dhar, T. Sundararajan, and S. K. Das, "Thermally "smart" characteristics of nanofluids in parallel microchannel systems to mitigate hot spots in MEMS," *IEEE Trans. Compon. Packag. Technol.*, vol. 6, no. 12, pp. 1834–1846, 2016. DOI: [10.1109/TCPMT.2016.2619939](https://doi.org/10.1109/TCPMT.2016.2619939).
- C. Anbumeenakshi, and M. R. Thansekhar, "Experimental investigation of header shape and inlet configuration on flow maldistribution in micro-channel," *Exp. Therm. Fluid Sci.*, vol. 75, pp. 156–161, 2016. DOI: [10.1016/j.expthermflusci.2016.02.004](https://doi.org/10.1016/j.expthermflusci.2016.02.004).
- S. R. Reddy, and G. S. Dulikravich, "Inverse design of cooling arrays of micro pin-fins subject to specified coolant inlet temperature and hot spot temperature," *Heat Transf. Eng.*, vol. 38, no. 13, pp. 1147–1156, 2017. DOI: [10.1080/01457632.2016.1239924](https://doi.org/10.1080/01457632.2016.1239924).
- C. S. Sharma *et al.*, "A novel method of energy efficient hotspot-targeted embedded liquid cooling for

- electronics: An experimental study,” *Int. J. Heat Mass Transf.*, vol. 88, pp. 684–694, 2015. DOI: [10.1016/j.ijheatmasstransfer.2015.04.047](https://doi.org/10.1016/j.ijheatmasstransfer.2015.04.047).
27. F. Alfieri *et al.*, “Computational modelling of hot spot identification and control in 3D stacked chips with integrated cooling,” *Numer. Heat Transf. Part A*, vol. 65, no. 3, pp. 201–215, 2014. DOI: [10.1080/10920277.2013.826480](https://doi.org/10.1080/10920277.2013.826480).
  28. J. Zhang, T. Zhang, S. Prakash, and Y. Jaluria, “Experimental and numerical study of transient electronic chip cooling by liquid flow in microchannel heat sinks,” *Numer. Heat Transf. Part A*, vol. 65, no. 7, pp. 627–643, 2014. DOI: [10.1080/10407782.2013.846594](https://doi.org/10.1080/10407782.2013.846594).
  29. C. Kinkelin *et al.*, “Theoretical and experimental study of a thermal damper based on a CNT/PCM composite structure for transient electronic cooling,” *Energy Convers. Manag.*, vol. 42, pp. 257–271, 2017. DOI: [10.1016/j.enconman.2017.03.034](https://doi.org/10.1016/j.enconman.2017.03.034).
  30. A. Bar-Cohen, M. Arik, and M. Ohadi, “Direct liquid cooling of high flux micro and nano electronics components,” *Proc. IEEE*, vol. 94, no. 8, pp. 1549–1570, 2006. DOI: [10.1109/JPROC.2006.879791](https://doi.org/10.1109/JPROC.2006.879791).
  31. A. M. A. Soliman, and H. Hassan, “3D study on the performance of cooling technique composed of heat spreader and microchannels for cooling the solar cells,” *Energy Convers. Manag.*, vol. 170, pp. 1–18, 2018. DOI: [10.1016/j.enconman.2018.05.075](https://doi.org/10.1016/j.enconman.2018.05.075).
  32. M. A. Soliman, H. Hassan, M. Ahmed, and S. Oakawara, “A 3D model of the effect of using heat spreader on the performance of photovoltaic panel (PV),” *Math. Comput. Simul.*, 2018. DOI: [10.1016/j.matcom.2018.05.011](https://doi.org/10.1016/j.matcom.2018.05.011).
  33. Y. Lee, S. Park, C. Byun, and S. K. Lee, “Liquid cooling of laser-driven head light employing heat spreader manufactured by 3D metal printing,” *Int. J. Precis. Eng. Manuf.-Green Tech.*, vol. 5, no. 2, pp. 295–301, 2018. DOI: [10.1007/s40684-018-0031-8](https://doi.org/10.1007/s40684-018-0031-8).
  34. B. Kelly, Y. Hayashi, and Y. J. Kim, “Novel radial pulsating heat pipe for high heat flux thermal spreading,” *Int. J. Heat Mass Transf.*, vol. 121, pp. 97–106, 2018. DOI: [10.1016/j.ijheatmasstransfer.2017.12.107](https://doi.org/10.1016/j.ijheatmasstransfer.2017.12.107).
  35. Y. Han, B. L. Lau, G. Tang, and X. Zhang, “Thermal management of hotspots using diamond heat spreader on Si-micro cooler for GaN devices,” *IEEE Trans. Compon. Package. Technol.*, vol. 5, no. 5, 2015.
  36. L. S. Maganti, P. Dhar, T. Sundarajan, and S. K. Das, “Mitigating non-uniform heat generation induced hotspots in multicore processor using heat generation induced hotspots in multicore processor using nanofluids in parallel microchannels,” *Int. J. Therm. Sci.*, vol. 125, pp. 185–196, 2018. DOI: [10.1016/j.ijthermalsci.2017.11.015](https://doi.org/10.1016/j.ijthermalsci.2017.11.015).
  37. P. Wang, B. Yang, and A. Bar-Cohen, “Mini-contact enhanced thermoelectric coolers for on-chip hotspot cooling,” *Heat Transf. Eng.*, vol. 30, no. 9, pp. 736–743, 2009. DOI: [10.1080/01457630802678391](https://doi.org/10.1080/01457630802678391).
  38. A. Bar-Cohen, and P. Wang, “Thermal management of on-chip hotspot,” *J. Heat Transf.*, vol. 134, no. 5, pp. 05107, 2012.
  39. D. Ansari, and K. Y. Kim, “Hotspot thermal management using a microchannel-pinfin hybrid heat sink,” *Int. J. Thermal Sci.*, vol. 134, pp. 27–39, 2018. DOI: [10.1016/j.ijthermalsci.2018.07.043](https://doi.org/10.1016/j.ijthermalsci.2018.07.043).
  40. Y. Pi, J. Chen, M. Miao, Y. Jin, and W. Wang, “A fast and accurate temperature prediction method for microfluidic cooling with multiple distributed hotspots,” *Int. J. Heat Mass Transf.*, vol. 127, pp. 1223–1232, 2018. DOI: [10.1016/j.ijheatmasstransfer.2018.07.127](https://doi.org/10.1016/j.ijheatmasstransfer.2018.07.127).
  41. K. P. Drummond, J. A. Weibel, S. V. Garimella, D. Black, D. B. Janes, and M. D. Sinanis, “Evaporative intrachip hotspot cooling with a hierarchical manifold microchannel heat sink array,” in *Thermal and Thermo mechanical Phenomenon in Electronic Systems, 2016*. Fifteenth Intersociety IEEE conference, Los Vegas, NV, USA, 31 May 2016, pp. 307–315.
  42. A. Abdoli, G. S. Dulikravich, G. Vasquez, and S. Rastkar, “Thermo-fluid stress-deformation analysis of two-layer microchannels for cooling chips with hotspots,” *J. Electron. Packag.*, vol. 137, no. 3, pp. 031003, 2015. DOI: [10.1115/1.4030005](https://doi.org/10.1115/1.4030005).
  43. D. Lorenzini, Y. K. Joshi, and G. W. Woodruff, “CFD study of flow boiling in silicon microgaps with staggered pin fins for 3D-stacking of ICS” in *Thermal and Thermo mechanical Phenomenon in Electronic Systems, 2016*. Fifteenth Intersociety IEEE conference, Los Vegas, NV, USA, 31 May 2016, pp. 766–773.
  44. Y. L. Lee, P. K. Singh, and P. S. Lee, “Fluid flow and heat transfer investigations on enhanced microchannel heat sink using oblique fins with parametric study,” *Int. J. Heat Mass Transf.*, vol. 81, pp. 325–336, 2015. DOI: [10.1016/j.ijheatmasstransfer.2014.10.018](https://doi.org/10.1016/j.ijheatmasstransfer.2014.10.018).
  45. C. Green, A. G. Fedorov, and Y. K. Joshi, “Fluid-to fluid spot-to-spreader (F2/S2) hybrid heat sink for integrated chip level and hot spot-level thermal management,” *J. Electron. Packag.*, vol. 131, no. 2, pp. 025002, 2009. DOI: [10.1115/1.3104029](https://doi.org/10.1115/1.3104029).
  46. W. S. Hummers, and R. E. Offeman, “Preparation of graphitic oxide,” *J. Am. Chem. Soc.*, vol. 80, no. 6, pp. 1339, 1958. DOI: [10.1021/ja01539a017](https://doi.org/10.1021/ja01539a017).
  47. M. Sreejesh, S. Dhanush, F. Rossignol, and H. S. Nagaraja, “Microwave assisted synthesis of rGO/ZnO composites for non-enzymatic glucose sensing and supercapacitor applications,” *Ceram. Int.*, vol. 43, no. 6, pp. 4895–4903, 2017. DOI: [10.1016/j.ceramint.2016.12.140](https://doi.org/10.1016/j.ceramint.2016.12.140).
  48. B. C. Pak, and Y. I. Cho, “Hydrodynamic and heat transfer study of dispersed fluids with submicron metallic oxide particle,” *Exp. Heat Transf.*, vol. 11, no. 2, pp. 151–170, 1998. DOI: [10.1080/08916159808946559](https://doi.org/10.1080/08916159808946559).
  49. Y. Xuan, and W. Roetzel, “Conceptions for heat transfer correlation of nanofluids,” *Int. J. Heat Mass Transf.*, vol. 43, no. 19, pp. 3701–3707, 2000. DOI: [10.1016/S0017-9310\(99\)00369-5](https://doi.org/10.1016/S0017-9310(99)00369-5).
  50. H. C. Brinkman, “The Viscosity of concentrated suspensions and solutions,” *J. Chem. Phys.*, vol. 20, no. 4, pp. 571, 1952. DOI: [10.1063/1.1700493](https://doi.org/10.1063/1.1700493).
  51. R. L. Hamilton, and O. K. Crosser, “Thermal conductivity of heterogeneous two-component systems,” *Ind. Eng. Chem. Fund.*, vol. 1, no. 3, pp. 187–191, 1962. DOI: [10.1021/i160003a005](https://doi.org/10.1021/i160003a005).
  52. T. T. Baby, and S. Ramaprabhu, “Enhanced convective heat transfer using graphene dispersed

- nanofluids,” *Nanoscale Res. Lett.*, vol. 6, no. 1, pp. 289–297, 2011.
53. H. W. Coleman, and W. G. Steele, *Experimentation, Validation and Uncertainty Analysis for Engineers*, 3rd ed. Hoboken, NJ: John Wiley & Sons, July 2009.
  54. M. Mirzaei, and A. Azimi, “Heat transfer and pressure drop characteristics of graphene oxide/water nanofluid in circular fitted with wire coil inserts,” *Exp. Heat Transf.*, vol. 29, no. 2, pp. 173–187, 2016. DOI: [10.1080/08916152.2014.973975](https://doi.org/10.1080/08916152.2014.973975).
  55. S. B. Choi, R. F. Barron, and R. O. Warrington, “Fluid flow and heat transfer in microtubes,” *Proc. ASME*, vol. 32, pp. 123–134, 1991.
  56. X. F. Peng, and G. P. Peterson, “Convective heat transfer and fluid friction for water flow in microchannel structures,” *Int. J. Heat Mass Transf.*, vol. 39, no. 12, pp. 2599–2608, 1996. DOI: [10.1016/0017-9310\(95\)00327-4](https://doi.org/10.1016/0017-9310(95)00327-4).
  57. B. X. Wang, and X. F. Peng, “Experimental investigation on liquid forced convection heat transfer through microchannel,” *Int. J. Heat Mass Transf.*, vol. 37, no. suppl. 1, pp. 73–82, 1994. DOI: [10.1016/0017-9310\(94\)90011-6](https://doi.org/10.1016/0017-9310(94)90011-6).
  58. J. Y. Jung, H. S. Oh, and H. Y. Kwak, “Forced convective heat transfer of nanofluids in microchannels,” *Int. J. Heat Mass Transf.*, vol. 52, no. 1–2, pp. 466–472, 2009. DOI: [10.1016/j.ijheatmasstransfer.2008.03.033](https://doi.org/10.1016/j.ijheatmasstransfer.2008.03.033).
  59. W. Qu, Gh, M. Mala, and D. Li, “Heat transfer for water in trapezoidal silicon microchannel,” *Int. J. Heat Mass Transf.*, vol. 43, no. 21, pp. 3925–3936, 2000. DOI: [10.1016/S0017-9310\(00\)00045-4](https://doi.org/10.1016/S0017-9310(00)00045-4).
  60. X. F. Peng, B. X. Wang, G. P. Peterson, and H. B. Ma, “Experimental investigation of heat transfer in flat plates with rectangular microchannels,” *Int. J. Heat Mass Transf.*, vol. 38, no. 1, pp. 127–137, 1995. DOI: [10.1016/0017-9310\(94\)00136-J](https://doi.org/10.1016/0017-9310(94)00136-J).
  61. P. Rosa, T. G. Karayiannis, and M. W. Collins, “Single-phase heat transfer in microchannels: The importance of scaling effects,” *Appl. Therm. Eng.*, vol. 29, no. 17–18, pp. 3447–3468, 2009. DOI: [10.1016/j.applthermaleng.2009.05.015](https://doi.org/10.1016/j.applthermaleng.2009.05.015).
  62. M. Asadi, G. Xie, and B. Sunden, “A review of heat transfer and pressure drop characteristics of single and two-phase microchannels,” *Int. J. Heat Mass Transf.*, vol. 79, pp. 34–53, 2014. DOI: [10.1016/j.ijheatmasstransfer.2014.07.090](https://doi.org/10.1016/j.ijheatmasstransfer.2014.07.090).
  63. W. Yu, and H. Xie, “A review on nanofluids: Preparation, stability, mechanisms and applications,” *J. Nanomater.*, vol. 2012, no. 435873, pp. 1–17, 2011. DOI: [10.1155/2012/435873](https://doi.org/10.1155/2012/435873).
  64. S. K. Das, S. U. S. Choi, and H. E. Patel, “Heat transfer in nanofluid- A review,” *Heat Transf. Eng.*, vol. 27, no. 10, pp. 3–19, 2006. DOI: [10.1080/01457630600904593](https://doi.org/10.1080/01457630600904593).
  65. A. Ebrahmi, F. Rikhtegar, A. Sabaghan, and E. Roohi, “Heat transfer and entropy generation in a microchannel with longitudinal vortex generators using nanofluids,” *Energy*, vol. 101, pp. 190–201, 2016. DOI: [10.1016/j.energy.2016.01.102](https://doi.org/10.1016/j.energy.2016.01.102).
  66. H. Zhang, S. Shao, H. Xu, and C. Tian, “Heat transfer and flow features of Al<sub>2</sub>O<sub>3</sub>-water nanofluids flowing through a circular microchannel- Experimental results and correlations,” *Appl. Therm. Eng.*, vol. 61, no. 2, pp. 86–92, 2013. DOI: [10.1016/j.applthermaleng.2013.07.026](https://doi.org/10.1016/j.applthermaleng.2013.07.026).